

REVIEWS OF TOPICAL PROBLEMS PACS numbers: **05.45.–a**, 43.30.Bp, 43.30.Cq, 43.30. Dr

Ray and wave chaos in underwater acoustic waveguides

A L Virovlyansky, D V Makarov, S V Prants

DOI: 10.3367/UFNe.0182.201201b.0019

Contents

Abstract. In the 1990s, the study of the chaotic behavior of ray trajectories in inhomogeneous waveguides emerged as a new field in ocean acoustics. It turned out that at ranges on the order of or larger than 1000 km ray chaos is well developed and should be taken into account when describing long-range sound propagation in the ocean. The theoretical analysis of ray chaos and of its finite-wavelength manifestation, wave chaos, is to a large extent based on well-known methods and ideas from the theory of dynamical and quantum chaos. Concrete examples are used to review the results obtained in this field over the last two decades.

1. Introduction

The transmission of sound in the ocean over distances of several hundred or even thousand kilometers owes its existence to the refractional waveguide of natural origin, called the underwater sound channel (USC) [1–3]. The vertical sound speed profile in deep USCs usually attains a minimum at a depth of approximately 1 km. As a consequence, sound energy appears to be partly trapped in the waveguide, which prevents it from strong attenuation on reflection from the absorbing bottom. Experiments on long-range sound transmission are most frequently carried out with sound waves at frequencies on the order of 100 Hz, which experience but negligible dissipation in sea water (only several decibels every 1000 km). For this reason, signals at such frequencies yield to reliable detection even at distances in excess of 10,000 km [4].

A L Virovlyansky Institute of Applied Physics, Russian Academy of Sciences, ul. Ul'yanova 46, 603950 Nizhny Novgorod, Russian Federation
D V Makarov, S V Prants Pacific Oceanological Institute, Far Eastern Branch of the Russian Academy of Sciences,
ul. Baltiiskaya 43, 690041 Vladivostok, Russian Federation
E-mail: prants@poi.dvo.ru

Received 15 March 2011, revised 29 April 2011
Uspekhi Fizicheskikh Nauk **182** (1) 19 – 48 (2012)
DOI: 10.3367/UFNr.0182.201201b.0019
Translated by S D Danilov; edited by A Radzig

The wave field in a USC satisfies the ordinary linear wave equation. To describe it, one may utilize the well-known methods traditionally used to analyze fields in waveguides of various physical natures.

Intensive theoretical and experimental studies of the long-range sound transmission in the ocean have been carried out now for more than sixty years. The issue has been considered well-studied already in the mid-1980s. Later, however, it transpired that there is a factor neglected previously, which to a large degree determines the structure of sound fields on distances of thousands of kilometers, namely ray chaos, the role of which in ocean acoustics was recognized only at the beginning of the 1990s. An important contribution was made by S S Abdullaev and G M Zaslavsky [5–9], the results of whose work are summarized in the review [10] published by *Physics–Uspekhi* in 1991 (see also the monograph [11]). Although the aforementioned work deals with the analysis of general questions pertaining to chaotic ray dynamics in inhomogeneous waveguides, to a substantial degree they have initiated active research on chaotic phenomena as applied to underwater acoustics tasks. At approximately the same time (the end of the 1980s–beginning of the 1990s), a series of articles were published in the USA which, in fact, launched systematic studies of ray and wave chaos in deep USCs [12–15].

In this review our goal is to introduce the reader to the results obtained in this area over the past 20 years. Not having the possibility (because of size limitations) of offering a complete account of relevant research, we will touch largely on those questions that have been solved with our direct participation. We try to compensate for the necessary brevity of our exposition by proposing an extended bibliography of work dedicated to the issue discussed here.

The essence of the ray chaos phenomenon is that a ray trajectory described by deterministic Hamiltonian equations behaves similarly to a random process. Chaotic trajectories are exceedingly sensitive to small variations in the initial conditions: the difference in the vertical coordinates (depths) z of two trajectories with close initial conditions grows (on average) with the distance r approximately according to the exponential law [10, 16–18]

$$\Delta z \sim \exp(\nu r) , \tag{1}$$

where ν is the so-called Lyapunov exponent. The difference in ray grazing angles grows according to a similar law (with the same ν). Estimates show that in realistic models of USCs the exponent ν reaches a magnitude on the order of 0.01 km^{-1} [16, 19]. At distances in excess of 1000 km, chaos is already well developed, and accounting for it becomes of principal importance. Studies of the ray chaos and its manifestations for a finite wavelength — *the wave chaos* — is currently considered to be one of components of the theory of long-range sound transmission in the ocean [20].

The phenomena of ray and wave chaos have well-known 'prototypes' in mechanics, exemplified, respectively, by dynamical and quantum chaos [21–25]. The point is that a ray trajectory in an inhomogeneous waveguide obeys the same Hamiltonian equations as a nonlinear oscillator under the action of a nonstationary (deterministic) external force. A typical situation occurs when the oscillator behaves quasi-randomly [26, 27]. An analysis of the phase space structure of such an oscillator presents the classical task in the dynamical chaos theory. The subjects of study in the quantum chaos theory are systems the classical analogs of which demonstrate chaotic behavior. A nonlinear oscillator excited by a nonstationary external force also falls into this category. Its wave function obeys the Schrödinger equation that coincides in form with the parabolic equation defining sound field in a waveguide.

The above analogy with a nonlinear oscillator invites one to apply the methods of dynamical and quantum chaos theory in studies of acoustic fields. However, the coincidence of primary equations notwithstanding, problem statements pertaining to the analysis of chaos in mechanics and acoustics are not infrequently substantially different. For instance, one of the main subjects of interest in ocean acoustics is the time of sound travel along a ray trajectory, which for brevity is dubbed the *ray travel time* [16, 19, 28–32]. The analog of this quantity in mechanics — Hamilton's principal function (also the action) — is not commonly measured in experiments and, hence, has not received a specific focus in the dynamical theory of chaos. We will see in what follows that it is very difficult to find a natural mechanical analog for the pulse signal field.

The horizontal scales of medium parameter variations in the ocean typically exceed the vertical scales by two orders of magnitude [33]. The horizontal refraction of acoustic waves can, therefore, be neglected in many cases. Adopting this approximation, we will consider below an axisymmetric (in fact two-dimensional) model of a medium in which the speed of sound c depends on only two coordinates: distance r, and depth z. We write out the sound speed field $c(r, z)$ as [19, 33]

$$c(r, z) = \bar{c}(z) + \delta c(r, z) , \tag{2}$$

where $\bar{c}(z)$ is the unperturbed smooth profile, and $\delta c(r, z)$ is a small perturbation thereof responsible for the origin of chaos. The exploration of ray chaos in underwater acoustics began from the analysis of waveguides with a periodic dependence of δc on the distance [10, 12, 14]. Such a selection of the perturbation type was motivated by the possibility of directly adapting the known results from the dynamical theory of chaos. Despite the apparently artificial character of the periodic model, it helped uncover a set of general features related to chaotic ray dynamics, which remain relevant in waveguides with realistic inhomogeneities as well.

An example of a fairly realistic model is furnished by a waveguide with the perturbation $\delta c(r, z)$ brought about by random internal-gravity waves (or simply internal waves, for brevity) with statistics obeying the Garrett–Munk spectrum [33]. Such a perturbation is typically dealt with when analyzing acoustic fields in deep seas in the framework of the theory of sound propagation in random media [33]. Note the crucial factor that this theory and that of ray and wave chaos study the fields in randomly inhomogeneous waveguides from different aspects complementing each other.

In the theory of wave propagation in random media, the description of rays (as well as other wave field characteristics) relies on the concept of a statistical ensemble of medium realizations. The statistical properties of a ray with given initial parameters z_0 and χ_0 — the initial depth and angle to the horizon, respectively — are found by averaging over rays with the same initial parameters for different medium realizations forming the ensemble. This is a traditional approach in underwater acoustics, and most studies dealing with the analysis of the stochastic ray field structure are carried out in its framework [33, 34].

Work exploring the ray chaos employs a different vantage point in its analysis of the impact of sound speed fluctuations $\delta c(r, z)$. The chaotic ray behavior is studied in a deterministic medium with spatial variations of sound speed set by a certain realization of the random perturbation $\delta c(r, z)$. Since for $r \gg \nu^{-1}$ the ray trajectories with close initial conditions are practically independent, averaging over the initial conditions can be treated as statistical averaging. Results of numerical modeling evidence that the statistical properties of chaotic rays found in this way only weakly depend on the concrete realization $\delta c(r, z)$ used in computations [35–37]. One can therefore expect that the analysis of ray statistics for a particular realization of the sound speed field will lead to results resembling those obtained by averaging over the ensemble of waveguides. Admittedly, the important and extremely interesting question of how well a single realization of inhomogeneities represents the statistical ensemble as a whole remains insufficiently studied.

The material in this review is arranged in the following way. Section 2 briefly discusses the methods of acoustic field description in the USC that will be used in this review. Section 3 lists the main types of ocean inhomogeneities which influence sound wave propagation. Section 4 explains the basic principle of acoustic monitoring of temperature fields in the ocean. It relies on the measurements of arrival times for sound pulses propagating along individual ray trajectories.

Here, we briefly review certain important experiments on long-range sound transmission in the ocean, the results of which lend support to the applicability of the ray description of sound fields to distances measuring thousands of kilometers. Section 5 is dedicated to the analysis of USC models with periodic inhomogeneities. It discusses wave chaos onset mechanisms for various relationships between inhomogeneity scales, and also chaos manifestations in the properties of wave dynamics. Section 6 turns to the ray and wave chaos in more realistic models of a USC characterized by sound speed fluctuations imposed by random internal waves. It presents the method of the statistical description of chaotic ray trajectories and shows how it can be applied to estimate the smoothed distribution of field intensity for a finite wavelength. A substantial portion of Section 6 is dedicated to the analysis of travel times for chaotic rays. It is also shown that because of the link between the ray and modal field representations in a waveguide the stochastic ray theory can be applied for the analysis of field mode structure under the conditions of wave chaos.

2. Basic equations

In this section we list the basic equations employed to describe sound fields in deep USCs. We also give definitions of the field characteristics used in Sections 3–6.

2.1 The Helmholtz equation and the parabolic equation

All internal motions in the ocean bulk are so slow that ocean inhomogeneities do not change much during the time it takes sound waves to cross them. This enables one to apply the approximation of frozen inhomogeneities, i.e., to treat the medium parameters as independent of time t. In what follows, we consider deep USCs with the sound speed field (2), where $\delta c(r,z)$ is a weak perturbation caused by random internal waves [1]. We assume the z-axis to be directed vertically downward, with the water surface on the horizon $z=0$. We also assume that the unperturbed sound speed profile $\bar{c}(z)$ has a single minimum at the horizon $z=z_{\mathrm{a}}$, which will be referred to as the USC axis. The sound pressure $\tilde{v}(r,z,t)$ is described by the linear wave equation

$$\frac{1}{c^2}\frac{\partial^2\tilde{v}}{\partial t^2}-\Delta\tilde{v}=0\,. \tag{3}$$

Its solutions can conveniently be written out in terms of the Fourier integral

$$\tilde{v}(r,z,t)=\int \mathrm{d}\Omega\, v(r,z,\Omega)\exp(-\mathrm{i}\Omega t)\,, \tag{4}$$

where $v(r,z,\Omega)$ obeys the Helmholtz equation [2, 3]

$$\frac{1}{r}\frac{\partial}{\partial r}\,r\,\frac{\partial v}{\partial r}+\frac{\partial^2 v}{\partial z^2}+\frac{\Omega^2}{c^2}\,v=0\,, \tag{5}$$

with appropriate boundary conditions.

Only waves propagating at small grazing angles χ and trapped by the USC survive at distances measuring from several hundred to a few thousand kilometers, which are of interest to us. Namely such waves are the subject of our study. In deep USCs typical at mid- and low latitudes, the grazing angles for waves propagating without interaction with the bottom (a typical ocean depth at these latitudes is about 5–6 km) do not exceed $14^\circ-16^\circ$. They can be described in the small-angle approximation. We write down v in the form

$$v(r,z,\Omega)=r^{-1/2}u(r,z,\Omega)\exp(\mathrm{i}kr)\,, \tag{6}$$

where $k=\Omega/c_0$ is the wave number in a homogeneous medium with a constant sound speed c_0, which is approximately equal to the mean sound speed in the USC, and $u(r,z,\Omega)$ is the smooth envelope of complex-valued field amplitude. The argument Ω of function $u(r,z,\Omega)$ will be omitted if we are dealing with a monochromatic source. Substituting Eqn (6) in Eqn (5) and neglecting the second derivative of u with respect to r, we arrive at the so-called standard parabolic equation [38–40]

$$2\mathrm{i}k\,\frac{\partial u}{\partial r}+\frac{\partial^2 u}{\partial z^2}-2k^2\big[U(z)+V(r,z)\big]u=0\,, \tag{7}$$

where

$$U(z)=\frac{1}{2}\left(1-\frac{c_0^2}{\bar{c}^2(z)}\right),\qquad V(r,z)\simeq\frac{\delta c(r,z)}{c_0}\,. \tag{8}$$

A nonstationary wave field excited by a pulsed source can be synthesized from solutions to the parabolic equation (7) at different carrier frequencies according to the formula

$$v(r,z,t)=r^{-1/2}\int \mathrm{d}\Omega'\,u(r,z,\Omega')\,s(\Omega')\exp\left[\mathrm{i}\Omega'\left(\frac{r}{c_0}-t\right)\right], \tag{9}$$

where $s(\Omega)$ is the spectrum of the radiated sound pulse. It should be noted that equation (7) formally coincides with the Schrödinger equation of quantum mechanics. In this analogy, r plays the role of time, k^{-1} of the Planck constant, and $U+V$ of the potential. This quantum-mechanical analogy opens wide horizons for applying the method of dynamical and quantum chaos to the study of ray and wave chaos in USCs. It is noteworthy that the integration over Ω in Eqn (9) formally corresponds to the integration over the Planck constant. We meant namely this fact in the Introduction when mentioning difficulties with proposing a quantum-mechanical analog for a pulsed signal field.

2.2 The geometrical optics approximation and Hamilton's formalism

In the geometrical optics approximation, valid if the wavelength $\lambda=2\pi/k$ is small compared to the typical size of medium inhomogeneities L_{inh}, a solution to the parabolic equation (7) is sought in the form [2, 3, 41]

$$u=A\exp(\mathrm{i}kS)\,, \tag{10}$$

where $A(r,z)$ and $S(r,z)$ are the amplitude and ray eikonal, respectively. Both these functions are expressed through parameters of ray trajectories. We use Hamilton's formalism to describe the trajectories [10, 42, 43]. In its framework, the trajectory at each point at a distance r is characterized by its depth (vertical coordinate) z and generalized momentum (or simply momentum) p. In the small-angle approximation, $p=\tan\chi$, where χ is the ray grazing angle. The dependences of z and p on the distance are given by the Hamilton equations (ray equations)

$$\frac{\mathrm{d}p}{\mathrm{d}r}=-\frac{\partial H}{\partial z}\,,\qquad \frac{\mathrm{d}z}{\mathrm{d}r}=\frac{\partial H}{\partial p}\,, \tag{11}$$

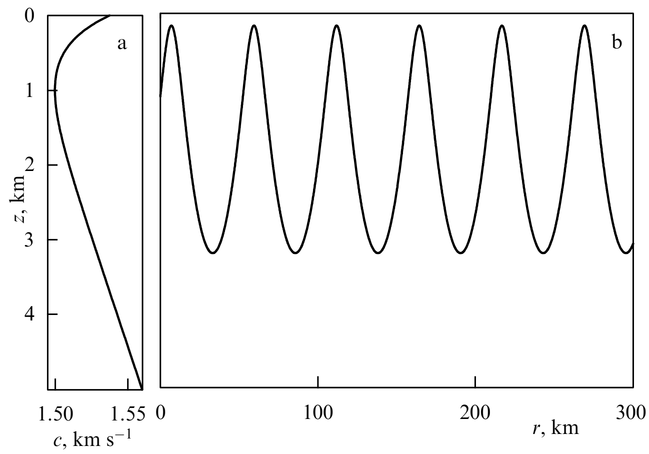

Figure 1. The canonical sound speed profile (a), and an example of ray trajectory in an unperturbed USC with this profile (b).

where $H(r, p, z)$ is the Hamiltonian of the ray system. In our case, it assumes the form

$$H(r, p, z) = H_0(p, z) + V(r, z)\,, \tag{12}$$

where

$$H_0(p, z) = \frac{p^2}{2} + U(z)\,. \tag{13}$$

Ray trajectories in an unperturbed (range-independent) USC are periodic, oscillating curves. An example of a trajectory, plotted in Fig. 1, is computed for a waveguide with the so-called canonical sound speed profile, also called the Munk profile [1, 2]

$$\bar{c}(z) = c_0\left\{1 + \epsilon\left[\exp\left(\frac{2(z_{\mathrm{a}} - z)}{z_{\mathrm{th}}}\right) + 2\,\frac{z - z_{\mathrm{a}}}{z_{\mathrm{th}}} - 1\right]\right\}, \tag{14}$$

where $c_0 = 1.5\ \mathrm{km\,s^{-1}}$, $z_{\mathrm{a}} = 1$ km, $\epsilon = 0.0057$, and $z_{\mathrm{th}} = 1$ km. The grazing angle of this trajectory on the waveguide axis — the depth corresponding to the minimum sound speed — equals 10°. The oscillation cycle length (period) is about 50 km, which is typical for a deep water USC.

The ray eikonal $S(r, z)$, which is a close analog to the action in mechanics [42], is expressed by the integral

$$S = \int (p\,\mathrm{d}z - H\,\mathrm{d}r)$$

computed along the ray trajectory.

In the two-dimensional medium considered here, the wave field is represented by a one-parametric family of ray trajectories $z(r, \alpha)$, where α is the parameter labeling the trajectories [41]. It can be shown that in the small-angle approximation the ray amplitude is given by [37, 43]

$$A = \frac{C}{\sqrt{|\partial z/\partial \alpha|}}\,, \tag{15}$$

where the coefficient C depends on the source. The geometrical optics approximation is violated at caustics where the derivatives $\partial z/\partial \alpha$ tend to zero.

Take as an example a monochromatic point source with coordinates $(0, z_{\mathrm{s}})$. The field excited by it is the solution of the parabolic equation (7) subject to the initial condition

$$u(0, z) = \delta(z - z_{\mathrm{s}})\,. \tag{16}$$

In the vicinity of the source the solution has the same form as in the homogeneous space with $c(r, z) = c_0$:

$$u(r, z) = \sqrt{\frac{k}{2\pi \mathrm{i} r}}\,\exp\left[\mathrm{i}k\,\frac{(z - z_{\mathrm{s}})^2}{2r}\right]. \tag{17}$$

Since all the rays emanate from one and the same point, α is naturally identified with the initial ray momentum p_0. Substituting Eqn (15) into Eqn (10) and comparing the result with Eqn (17), we find

$$A = \sqrt{\frac{k}{2\pi \mathrm{i}\,|\partial z/\partial p_0|}}\,. \tag{18}$$

A characteristic feature of waveguide propagation is its multipath character. As a rule, several rays reach the observation point. They are sometimes called eigenrays. The contribution from each of them is given by formula (10), and the complex-valued field amplitude is expressed as the sum

$$u(r, z) = \sum_j A_j \exp\left(\mathrm{i}kS_j - \mathrm{i}\mu_j\,\frac{\pi}{2}\right), \tag{19}$$

where the index j numbers the eigenrays, and μ_j is the number of contacts with caustics for the ray j (the Maslov index).

2.3 Ray travel times

In the geometrical optics approximation, the signal at some reception point represents a superposition of sound pulses, each arriving along one of the eigenrays. We term them the *ray* pulses. Their arrival times, called the ray travel times as mentioned in the Introduction, carry the main information needed for acoustical monitoring of ocean temperature fields (see Section 4). This is why their analysis occupies a prominent place in ocean acoustics.

There is a very simple connection between the ray travel time and the eikonal of a ray trajectory, which is elucidated upon substituting Eqn (10) in Eqn (9). The resulting expression defines the ray momentum. Since neither the trajectory parameters nor either function A or S depend on Ω, it can be readily seen that the ray travel time is

$$t = \frac{r + S}{c_0}\,. \tag{20}$$

To analyze the spatio-temporal structure of a pulsed signal at a given observation distance, ocean acoustics widely exploits the sound field characteristic called the $t-z$ diagram or timefront. The timefront is the distribution of ray travel times in the time–depth plane. An example of the $t-z$ diagram is presented in Fig. 2. The diagram is constructed for a point source in an unperturbed USC with the Munk profile (14) plotted in Fig. 1. Each point in the plot corresponds to the arrival time and depth of one of the rays at an observation distance of 400 km. Computations were performed for the rays leaving the point source located on the waveguide axis at the depth of 1 km and at grazing angles in the interval of $\pm 12°$.

The diagram, looking like two piecewise broken lines shifted relative each other along the time axis t, consists of segments, each formed by rays with the same identifiers $\pm M$,

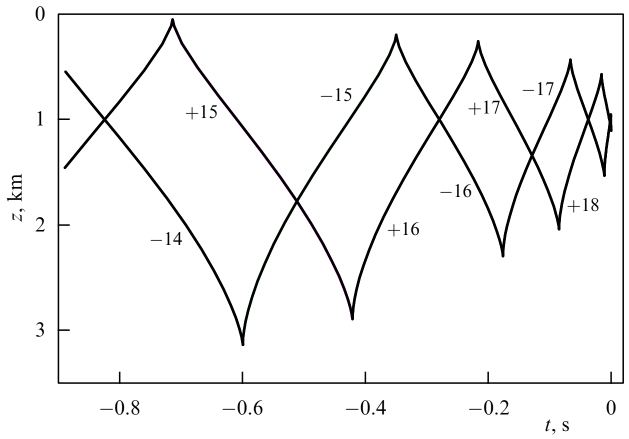

Figure 2. Timefront ($t-z$ diagram) presenting the distribution of ray travel times in a range-independent waveguide with the canonical sound speed profile (14) at a distance of 400 km. The diagram segments are labelled with identifiers of the rays forming them.

where $\pm$ is the sign of the angle at which the ray leaves the source, and M is the number of turning points of the ray trajectory. Such a shape of the $t-z$ diagram is typical for models of the USC that are range-independent or smoothly varying with distance. The number of diagram segments grows with the propagation distance, but the mean interval between them remains unchanged [37, 43].

We address the question about the distribution of chaotic ray arrivals in the time–depth plane in a perturbed USC in Section 6.4.

2.4 Action–angle variables

In the unperturbed (range-independent) waveguide with $V = 0$, the Hamiltonian $H = H_0$ remains constant along ray trajectories. The action variable in this case is defined as the integral along the oscillation cycle of the trajectory [10, 42]:

$$I = \frac{1}{2\pi}\oint p\,\mathrm{d}z = \frac{1}{\pi}\int_{z_{\min}}^{z_{\max}} \mathrm{d}z\,\sqrt{2\bigl[H_0 - U(z)\bigr]}\,, \tag{21}$$

where $z_{\min}$ and $z_{\max}$ are, respectively, the depths of the upper and lower ray turning points satisfying the condition $U(z) = H_0$. Formula (21) implicitly defines the function $H_0(I)$ expressing the dependence of the Hamiltonian on the action. The canonical transformation

$$p = p(I, \theta)\,, \qquad z = z(I, \theta)\,, \tag{22}$$

connecting the momentum–coordinate (p, z) and action–angle (I, θ) variables, is defined through the relationship

$$p = \frac{\partial G}{\partial z}\,, \qquad \theta = \frac{\partial G}{\partial I}\,, \tag{23}$$

where $G(I, z)$ is the generating function. For $p > 0$, one has

$$G(I, z) = \int_{z_{\min}}^{z} \mathrm{d}z\,P(I, z)\,, \qquad P(I, z) = \sqrt{2\bigl[H_0(I) - U(z)\bigr]}\,. \tag{24}$$

If $p < 0$, $G(I, z)$ should be replaced by the function $2\pi I - G(I, z)$. The angular variable θ defined in that way, varying within each ray period from 0 to 2π, is interpreted as the phase of the ray trajectory. It should not be confused with the ray grazing angle. In order to make θ a continuous function of distance r, it has to be incremented by 2π at the beginning of each new ray cycle [42]. In agreement with Liouville's theorem, the Jacobian of any canonical transformation is equal to unity [42], hence, one finds

$$\frac{\partial\bigl(I(p, z), \theta(p, z)\bigr)}{\partial(p, z)} = \frac{\partial\bigl(p(I, \theta), z(I, \theta)\bigr)}{\partial(I, \theta)} = 1\,. \tag{25}$$

The canonical transformation introduced for the unperturbed waveguide can also formally be used in the presence of perturbation. For $V \neq 0$, the ray equations take the form

$$\frac{\mathrm{d}I}{\mathrm{d}r} = -\frac{\partial V}{\partial \theta}\,, \tag{26}$$

$$\frac{\mathrm{d}\theta}{\mathrm{d}r} = \omega + \frac{\partial V}{\partial I}\,, \tag{27}$$

where $\omega(I) = \mathrm{d}H_0(I)/\mathrm{d}I$ is the spatial angular frequency of ray trajectory in the unperturbed waveguide. The cycle length of the unperturbed ray is $D(I) = 2\pi/\omega(I)$.

In what follows, we will apply the functions $I(r, I_0, \theta_0)$ and $\theta(r, I_0, \theta_0)$ to denote the action variable and ray angle coordinate at the distance r. The arguments I_0 and θ_0 are the initial values of these coordinates at $r = 0$. Sometimes, using analogous functions $I(r, p_0, z_0)$ and $\theta(r, p_0, z_0)$ is more convenient. Here, p_0 and z_0 are the initial values for the ray momentum and coordinate, respectively.

2.5 Modal representation of a wave field

At any distance r, the wave field can be represented as a series

$$u(r, z) = \sum_m a_m(r)\,\varphi_m(z)\,, \tag{28}$$

where $\varphi_m(z)$ are the eigenfunctions of the Sturm–Liouville problem in the unperturbed waveguide [2, 44]. Each term of sum (28) describes a normal mode. For simplicity, we limit ourselves to the analysis of contributions from those modes both of whose turning points are located inside the water depth. In the Wentzel–Kramers–Brillouin approximation, the mth eigenfunction is fully determined by the parameters of an unperturbed ray trajectory, with the action variable (denoted as I_m) satisfying the quantization rule [2, 44, 45]

$$kI_m = m - \frac{1}{2}\,, \quad m = 1, 2, \ldots\,. \tag{29}$$

In the depth interval between the turning points the mth eigenfunction can be represented as [2, 44, 45]

$$\varphi_m(z) = \varphi_m^+(z) + \varphi_m^-(z)\,, \tag{30}$$

where

$$\varphi_m^{\pm}(z) = \bigl[D(I_m)\,P(I_m, z)\bigr]^{-1/2} \exp\left\{\pm\mathrm{i}\left[kG(I_m, z) - \frac{\pi}{4}\right]\right\}. \tag{31}$$

2.6 Ray approach to the description of the field mode structure

The ray approach to the computation of mode amplitudes $a_m(r)$ in an inhomogeneous waveguide ($V \neq 0$) consists in expanding the field ray representation (19) in normal modes and computing the resultant integrals by the stationary phase method. A detailed discussion of this question is proposed by Refs [37, 43, 46–48]. It turns out that each mode is formed by contributions of rays — we call them *modal rays* — the actions of which on the observation distance r satisfy the condition

$$I(r, I_0, \theta_0) = I_m \, . \tag{32}$$

The parameters I_0 and θ_0 are interrelated, the relationship between them being determined by the source generating the field. It should be emphasized that for a given m the quantity I_m depends on the carrier frequency Ω and, for different Ω, condition (32) singles out different rays.

As a simple example consider a situation where only a single mode with a number m_0 is excited at the initial point of transmission, viz.

$$u(0, z) = \varphi_{m_0}(z) \, . \tag{33}$$

The rays forming the field $u(r, z)$ emerge from all depths z_0 between the turning points of the given mode. They all share the same initial value of the action variable equal to I_{m_0}. Since a mode is the superposition of two quasiplane waves [the so-called Brillouin waves given by the functions $\varphi_m^+(z)$ and $\varphi_m^-(z)$], two rays with initial momenta $p_0 = \pm P(I_{m_0}, z_0)$ emanate from each point. Condition (32) in this example attains the form

$$I(r, I_{m_0}, \theta_0) = I_m \, . \tag{34}$$

Condition (34) defines the values of θ_0 (and hence z_0) that correspond to modal rays. The contribution of a single modal ray to the mode amplitude a_m has the form [37, 43, 47–49]

$$a_m(r) = Q \exp\left[\mathrm{i}(\Phi + \beta)\right] , \tag{35}$$

where

$$Q = \frac{1}{\sqrt{2\pi k |\partial I(r, I_{m_0}, \theta_0)/\partial\theta_0|}} \exp\left[\pm \mathrm{i} k G(I_{m_0}, z_0)\right] , \tag{36}$$

$$\Phi = k\left[S(r, Z_m) + \sigma G(I_m, Z_m)\right] . \tag{37}$$

Here, Z_m is the depth of a modal ray at the distance of observation, $S(r, Z_m)$ is its eikonal, $\sigma = -\operatorname{sgn} p$, p is the modal ray momentum, and β is a constant independent of frequency.

Making use of the relationships written above, one can compute the mode amplitude in close analogy with the procedure applied to compute the field at a given waveguide point. First, the parameters of modal rays (analogs of eigenrays) are determined from condition (32). If there are several such rays, the mode amplitude is computed by summing their contributions. In a similar fashion, one can compute amplitudes of modes generated by a point source [37, 43, 47–49].

The approach discussed here establishes the link between the field ray and modal representation in a range-dependent waveguide with distance. With its assistance, the results obtained for ray dynamics in the presence of perturbation δc can be applied to the analysis of mode amplitude variations caused by this perturbation.

3. Internal waves and other inhomogeneities in the ocean

In modern ocean acoustics it is generally acknowledged that the main factor causing chaotic behavior of ray trajectories in the deep water is sound speed fluctuations induced by random internal waves [1, 19]. In spite of their fairly small amplitude, $\delta c/c_0 \simeq 5 \times 10^{-4}$, sound field distortions caused by them accumulate as the sound waves propagate and become noticeable already at distances of about 100 km. These fluctuations can be estimated [50] by relying on the model of the Garrett–Munk spectrum for internal wave perturbations [1, 50, 51]:

$$\frac{\delta c}{c_0} = \frac{\mu}{g} \, N^2(x, y, z) \, \zeta(x, y, z) \, , \tag{38}$$

where $\mu = 24.5$, N is the buoyancy frequency attaining a maximum at the thermocline depth, and $\zeta(x, y, z)$ describes vertical displacements of fluid parcels in the internal wave. This function is expressed as a superposition of modes of internal waves with random amplitudes whose statistics are given by the empirical Garrett–Munk spectrum. The variance of sound speed fluctuations caused by internal waves reduces with depth. Close to the surface, the root-mean-square value of δc is on the order of 1 m s^{-1}. The random field of internal waves in the ocean contains a large number of modes. Their horizontal periods vary from several hundred meters to several hundred kilometers, and the vertical periods from several dozen to several hundred meters. Spectral weights of higher modes are rather small, and yet they are responsible for the fine structure of the sound speed field. Analytical estimates and numerical simulations indicate that the field parameters computed with the assistance of this model agree well with the actual results of field measurements at distances measuring a few hundred or even a few thousand kilometers [1, 52].

It is noteworthy that the aforementioned model takes into account only the contributions from background internal-gravity waves, which can be described in the linear approximation. Alongside them, trains of intense nonlinear internal waves which do not follow the Garrett–Munk spectrum are not uncommon in the ocean. Their influence can be instrumental in the shelf zones of the ocean at relatively short sound paths (several dozen kilometers) [53, 54].

There are other factors in the ocean that may affect the sound propagation speed. One of them pertains to the influence of Rossby waves occurring because of the dependence of the Coriolis force on the latitude. These are planetary waves propagating largely from eastern to western coasts. Their horizontal scale is about several hundred kilometers, with vertical displacements on the order of 10 cm, and periods from several days for barotropic waves to months or years for baroclinic waves. In contrast to internal-gravity waves, Rossby waves can be treated as periodic or quasiperiodic perturbations and modelled as a superposition of several modes.

Large-scale ocean currents like the Gulf Stream or Kuroshio substantially modulate the sound speed profile for ray trajectories crossing them: the depth of the USC-axis changes, and a common type of USC may split in two or fully disappear. These currents meander and spawn eddies (rings) which scatter sound waves. The edges of these currents, so-called fronts, characterized by large gradients of hydrological parameters, cause refraction and backscattering of sound. The fronts are the regions of vigorous turbulent mixing of water masses with different temperatures and salinities, which leads to diffraction scattering of sound waves.

In addition to the localized currents, the ocean hosts other coherent structures that essentially affect the long-range sound transmission, such as the so-called synoptic eddies — mesoscale inhomogeneities in the ocean with typical horizontal scales from several dozen to several hundred kilometers. These eddies are drifting cyclonic or anticyclonic vortical structures with, respectively, a cold or warm core. They are ubiquitous in the ocean and have lifetimes from several months to more than a year. A characteristic vertical size of synoptic eddies ranges from a few hundred meters to more than one kilometer. The temperature contrast between the water inside the eddy and the ambient water implies strong inhomogeneities in the sound speed field, which can be reasonably described by a two-dimensional model [43]. The ocean also hosts topographic eddies — quasistationary formations of a synoptic size developing over underwater mountains or troughs.

The presence of strong large-scale inhomogeneities requires in some cases taking into account the three-dimensional structure of sound speed perturbations. Their spatial scales, however, are commonly so large that their role in the origin of chaotic dynamics of rays is rather modest. Such inhomogeneities, therefore, are not considered in this review. Nor do we consider the impact of surface waves. The subject of our study are waves trapped by a USC. They propagate at fairly small grazing angles and avoid reflections not only from the absorbing bottom but also from the rough ocean surface. It is assumed that fluctuations δc of the speed of sound are solely due to the internal waves.

4. Acoustic thermometry and experiments on long-range sound propagation in the ocean

Studies of long-range sound propagation in the ocean aim, first of all, to resolve issues concerning the acoustic monitoring of the temperature field in the water column. Temperature variations give rise to perturbation of the speed of sound δc, which then leads to variations of sound field. Long-term measurements of the sound field parameters make the reconstruction of variations in δc, in principle, possible (through the solution of the relevant inverse problem). They are then readily recast in terms of temperature variations. Acoustical monitoring offers a number of advantages over other remote sounding methods. For example, the abilities of satellite remote sensing are limited to the surface layer, whereas with the help of sound waves one may penetrate into the depths of the ocean.

The most known scheme of acoustical monitoring — the method of ocean acoustic tomography — was proposed in the seminal work of Munk and Wunsch [55]. The Munk–Wunsch approach relies on the fact that sound pulses arriving along various rays at a signal reception point can be fairly well resolved if the distance is sufficiently large. Moreover, their arrival times are predicted with reasonable accuracy in the framework of a simple medium model which neglects fluctuations in the speed of sound caused by internal waves and other relatively small-scale inhomogeneities.

The procedure of solving the inverse problem in the acoustic tomography method is based on the following simple considerations. Let us write out the sound speed field in the form $c(x,y,z) = c_{\mathrm{ref}}(x,y,z) + \delta c(x,y,z)$, where $c_{\mathrm{ref}}(x,y,z)$ is some reference field for the water area under study, which is constructed from long-term observational data (the information is retrieved from appropriate databases), and $\delta c(x,y,z)$ is the sought-for perturbation of this field. If the perturbation is not very large, then, in the first approximation, we can assume that it will not noticeably deflect the ray trajectories. The anomaly in the ray travel time δt is expressed as [55]

$$\delta t = -\int_{\Gamma} \frac{\delta c}{c_{\mathrm{ref}}^2}\, \mathrm{d}s\,, \tag{39}$$

where the integration is performed along the unperturbed trajectory Γ, and $\mathrm{d}s$ is an element of arc length. Formula (39) expresses the link between the unknown perturbation δc and measured anomalies δt in the ray travel time necessary for the solution to the inverse problem. Reference [55] proposed a method to solve the inverse problem, which was further advanced later in numerous studies by other authors (see the monograph [56] and references cited therein).

The Munk–Wunsch method was tested in a demonstration experiment carried out in the Atlantic in 1981 over a water area measuring 300×300 km^2 [57]. The estimates obtained in it agreed well with the results of direct measurements of the temperature field variations performed by contact methods.

The ray chaos imposes severe limitations on the capabilities of the Munk–Wunsch method. Indeed, the Munk–Wunsch scheme relies on computation of the family of eigenrays that connect the source and receiver of sound. Under the conditions of ray chaos, because of the extremely high sensitivity of trajectories to small variations in initial conditions, the number of eigenrays grows exponentially with distance, and the inverse problem becomes practically unsolvable at long paths [15].

Several authors proposed an analog to the method of ocean acoustic tomography called the method of modal tomography. The latter relies on using either the phases of complex-valued amplitudes of normal modes or travel times of acoustic pulses transferred by separate modes as observable acoustic parameters [58–60]. Variations in these parameters, just like variations in ray travel times, can simply be expressed in terms of perturbation δc. The modal tomography also suffers from limitations imposed by ray chaos: scattering on internal waves increases the duration of modal pulses, simultaneously modifying their shape in a rather irregular way [61, 62].

The acoustic tomography method has been proposed for the reconstruction of temperature perturbations over water areas with a typical size of several hundred (up to one thousand) kilometers. During the 1990s, the task of acoustic sounding over water areas measuring 5–10 thousand km (these are typical scales of ocean basins) emerged on the agenda. The aim was in diagnosing the variability in the mean ocean temperature on climate scales and in the analysis of greenhouse effect manifestations. The conclusion that this task is, in principle, solvable was made by analyzing the data of a set of large-scale marine experiments.

The best known and most impressive of such experiments was carried out in 1991 involving the joint efforts of an international team of scientists led by W Munk (USA) [4]. In this experiment, the sound signal from a coherent source was detected in different regions of the Atlantic and Pacific Oceans over an unprecedented distance of about 18 thousand kilometers (Fig. 3). It proved possible to resolve ray pulses with arrival times differing by just several milliseconds. This experiment became a test of the feasibility of acoustic signal detection at such long distances prior to planned work on the acoustic thermometry of the

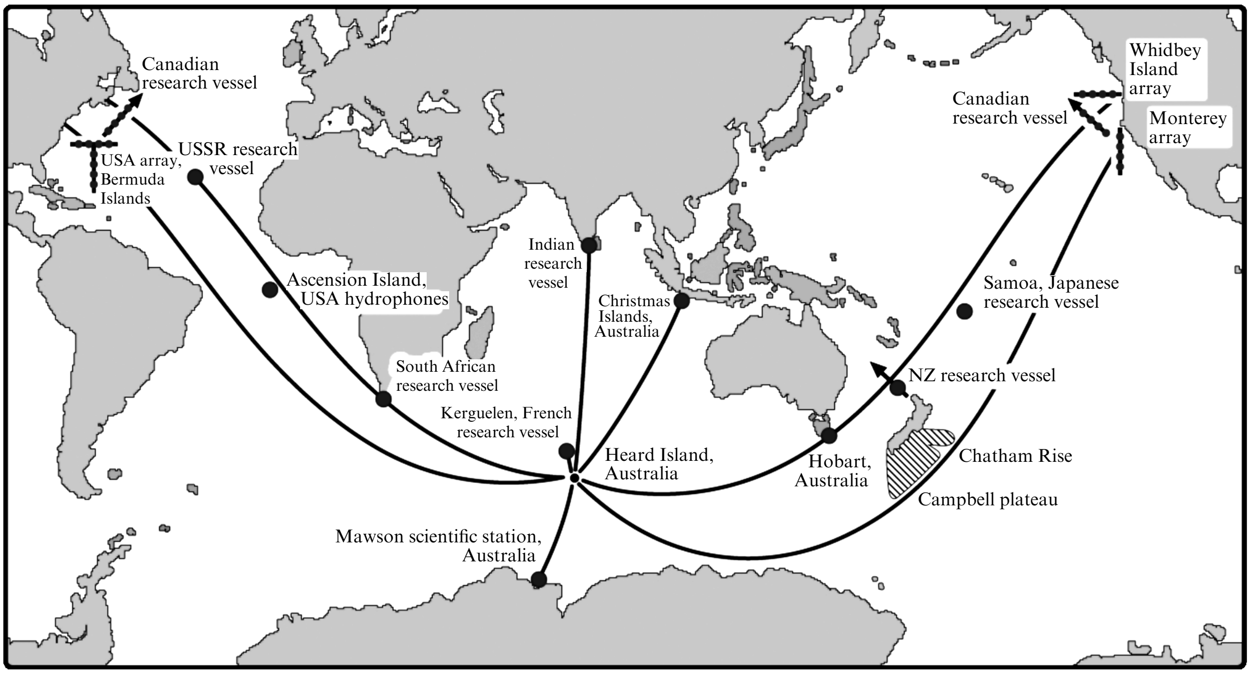

Figure 3. Layout of the experiment on long-range sound transmission in the ocean [4]. Dark circles indicate the positions of receiving systems.

ocean. The sound sources were disposed on the braid immersed from a research ship board to the depth of the local USC-axis (175 m) in the vicinity of Australia's Heard Island situated in the subantarctic zone of the Indian Ocean. Both monochromatic and narrow-band pulsed signals were studied at frequencies close to 60 Hz. The maximum radiated power reached 220 dB.

An important field experiment AET (Acoustic Engineering Test) was carried our during one week in November 1994. A broad-band source with a central frequency of 75 Hz was located in the North Pacific at a depth of 625 m near the axis of a USC. The signals were recorded near Hawaii with the help of a vertical braid composed of 20 receiving hydrophones. The distance between neighboring hydrophones was 35 m (1.75 of the wavelength at 75 Hz) and they covered a depth range from 900 to 1600 m. The acoustic path 3252 km in length did not cross large submarine ridges or large-scale hydrological features like fronts or currents.

The analysis of AET results was carried out in a series of papers [19, 63–65]. The initial part of the detected signal was rather stable and enabled the reliable arrival resolution and identification for pulses propagating along steep rays. The late part of the recorded signal, in contrast, was unstable, and did not exhibit any stable arrivals.

The qualitative difference between the early and late parts of the sound signal was explained with the help of ray chaos theory. Reference [19] reports on the results of numerical simulations of ray dynamics under conditions of the AET with account for internal-gravity waves characterized by the Garrett–Munk spectrum. They agree in general with the experimental results (Fig. 4). Simulations confirm that the divergence of trajectories with close initial conditions proceeds according to the law (1). The Lyapunov exponent ν was explored as a function of the grazing angle χ_0 at which the ray intersects the USC-axis. For flat rays ($|\chi_0| \leqslant 5^\circ$), a typical value of ν is $1/100\ \text{km}^{-1}$, while for steep rays ($6^\circ \leqslant \chi_0 \leqslant 11^\circ$) it drops to $1/300\ \text{km}^{-1}$. Thus, the steep rays are essentially less chaotic than their flat counterparts. This partly explains the stability of the initial part of the signal, as it is formed by contributions from steep rays.

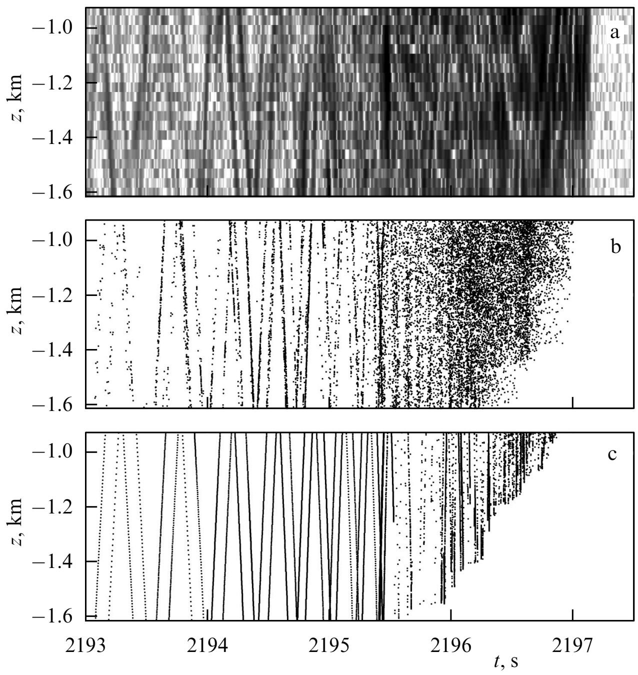

Figure 4. The measured and computed $t-z$ diagrams of the AET experiment. (a) Typical result of measuring the sound intensity with a dynamical range of 30 dB. (b) Computed $t-z$ diagram with account for internal-gravity waves. (c) The same, but without the internal-gravity waves [19]. (The vertical axis is directed upward, so that the ocean depth z takes negative values.)

A similar picture was observed in the SLICE89 experiment [66, 67] carried out on a path 1000 km in length in the north-east Pacific in 1989 by using a source at a frequency of 250 Hz and vertical antenna 3 km in length containing 50 hydrophones. Notice that the chaotic character of flat rays is not the general law of sound propagation in the deep ocean. For example, experiments carried out in the Sea of Japan with a source near the Gamov peninsula [68–70] indicate a high stability of nearly axial rays, which by all probability can be attributed to characteristics of internal waves in that region.

These and other field experiments proved that low-frequency acoustic signals can propagate over many thousands of kilometers experiencing rather small attenuation. It turned out that even on such long-range paths the important sound field characteristics can be well described in the framework of geometrical optics. In particular, sound pulses arriving at the observation point along steep rays and forming the initial part of the signal can in many cases be resolved and identified. Moreover, it is shown that long-term observation of arrival time variations allows one to monitor climatic variations of the mean temperature [71]. On the other hand, experiments indicate that sound speed fluctuations created by internal waves and other hydrological inhomogeneities essentially affect the long-range sound propagation. This emphasizes the necessity of accounting for ray chaos effects when properly considering sound transmission over large distances.

5. Ray and wave chaos in waveguides with periodic inhomogeneities

This section considers simplified models of USCs in which sound speed perturbations are periodic functions of the horizontal coordinate. We discuss the main mechanisms responsible for the emergence of ray chaos. The section explores the structure of the phase space for a periodic model and looks into manifestations of ray chaos at a finite wavelength. The assumption of periodic perturbation is undoubtedly a very strong idealization. In reality, the inhomogeneity of sound speed in the ocean is characterized by a broad spatial spectrum without separated peaks. In order to somewhat smooth over this contradiction, we offer to the readers attention an approach which allows one to apply certain results from the theory of periodically inhomogeneous waveguides to the analysis of chaotic ray dynamics in randomly inhomogeneous waveguides.

5.1 Chaos in waveguides with a smooth dependence of perturbation on the depth

5.1.1 Nonlinear resonance. Let us consider the most simple scenario for the origin of ray chaos in a USC. We depart from the ray Hamiltonian (12) and assume that the perturbation $V(r,z)$ can be represented in the following form

$$V(r,z) = V(r+\lambda_r, z) = \varepsilon \bar{V}(r,z)\,, \quad \varepsilon \ll 1\,, \tag{40}$$

where $\bar{V}$ is some 'slow' function of the vertical coordinate z. The ray Hamiltonian, expressed in the action–angle variables, takes the form

$$H = H_0(I) + \varepsilon \bar{V}(I,\vartheta,r)\,. \tag{41}$$

Expanding $\bar{V}$ in a double Fourier series, viz.

$$\bar{V}(I,\vartheta,r) = \sum_{l,m} \bar{V}_{l,m}(I) \exp\left[\mathrm{i}(l\vartheta - mk_r r)\right]\,, \tag{42}$$

we reduce the ray equations (26) and (27) to the form [40]

$$\frac{\mathrm{d}I}{\mathrm{d}r} = -\frac{\mathrm{i}\varepsilon}{2}\sum_{l,m} l\bar{V}_{l,m}(I)\exp\left[\mathrm{i}(l\vartheta - mk_r r)\right] + \text{c.c.}, \tag{43a}$$

$$\frac{\mathrm{d}\vartheta}{\mathrm{d}r} = \omega(I) + \frac{\mathrm{i}\varepsilon}{2}\sum_{l,m}\frac{\partial \bar{V}_{l,m}}{\partial I}\exp\left[\mathrm{i}(l\vartheta - mk_r r)\right] + \text{c.c.}, \tag{43b}$$

where $\bar{V}_{l,m}$ is the Fourier amplitude, $k_r = 2\pi/\lambda_r$, and c.c. stands for the complex conjugation. If the condition

$$l\omega(I) - mk_r = 0 \tag{44}$$

is satisfied, Eqns (43a) and (43b) exhibit resonance. It is similar to ordinary nonlinear resonance in classical mechanics (with the only difference being that the role of time is played by the horizontal coordinate r) and came to be known as spatial nonlinear resonance [10]. In what follows, the nonlinear resonance with $l = l^*$ and $m = m^*$ will be referred to as the $l^* : m^*$ resonance. Since condition (44) may hold for different combinations of l, m, and I, the resonances everywhere densely cover the phase space. However, only a small fraction of them pertaining to small values of l and m proves to be significant for the ray dynamics, because the Fourier amplitudes of the expansion (42) exhibit fast decay as the index of a harmonic increases.

Let us isolate the resonance with $l = l_0$, $m = m_0$, and $I = I_0$ and consider ray dynamics in its vicinity. Omitting off-resonance terms and substituting $\bar{V}_{l,m} = V_0 \exp(\mathrm{i}\psi_0)$, where $V_0 \in \mathbb{R}$, into Eqns (43a) and (43b), we find

$$\frac{\mathrm{d}I}{\mathrm{d}r} = \varepsilon l_0 V_0 \sin(l_0\vartheta - m_0 k_r r + \psi_0)\,, \tag{45a}$$

$$\frac{\mathrm{d}\vartheta}{\mathrm{d}r} = \omega(I) + \varepsilon\,\frac{\partial V_0}{\partial I}\cos(l_0\vartheta - m_0 k_r r + \psi_0)\,. \tag{45b}$$

Assuming that the deviation of action from the resonance value, $\Delta I = I - I_0$, is small, we may utilize the approximations $\omega(I) = \omega(I_0) + \omega'\Delta I$, where $\omega' = \mathrm{d}\omega/\mathrm{d}I$ and $V_0 = V_0(I_0)$. We also neglect the term of order ε on the right-hand side of equation (45b). As a result, we arrive at the following system of equations:

$$\frac{\mathrm{d}(\Delta I)}{\mathrm{d}r} = -\varepsilon l_0 V_0 \sin\Psi\,, \qquad \frac{\mathrm{d}\Psi}{\mathrm{d}r} = l_0\omega'\Delta I\,, \tag{46}$$

where the new variable $\Psi = l_0\vartheta - m_0 k_r r + \psi_0 - \pi$ was introduced. System of equations (46) corresponds to the Hamiltonian

$$\tilde{H} = \frac{1}{2}\, l_0\omega'(\Delta I)^2 - \varepsilon l_0 V_0 \cos\Psi\,. \tag{47}$$

Since this Hamiltonian formally coincides with that of a nonlinear pendulum, the trajectories of solutions to system (46) take the form of finite or infinite oscillations. Trapping into resonance corresponds to finite oscillations, where the magnitude of ray action I is localized within a narrow interval around $I = I_0$. Its width is given by the formula

$$\Delta I_{\max} = \sqrt{\frac{\varepsilon V_0}{|\omega'|}}\,. \tag{48}$$

The reduction of nonintegrable system of equations (43a) and (43b) to integrable system (46) is approximate and holds only under certain conditions. First, the condition of mild nonlinearity,

$$\varepsilon \ll \alpha \ll \varepsilon^{-1}\,, \tag{49}$$

must be satisfied. Here, α is the dimensionless nonlinearity parameter:

$$\alpha = \frac{|\omega'|I}{\omega}\,. \tag{50}$$

Second, the integrability is lost if resonances neighboring in the phase space overlap. This happens when the relation is fulfilled:

$$K = \frac{\Delta I_{\max}}{\delta I} \gtrsim 1\,, \tag{51}$$

where δI is the distance between the resonances in terms of action. Condition (51) is the Chirikov criterion [72]. For overlapping resonances, a chaotic sea forms in the phase space, which can be quite extended. If a ray belongs to the chaotic sea, its trajectory becomes irregular, while its action ceases to be a slowly varying quantity and can strongly deviate from its initial value.

The impact of resonance overlapping on the ray dynamics in a horizontally periodic waveguide can be visualized with the help of a Poincaré map:

$$\begin{aligned} p_{m+1} &= p(r = \lambda_r | p_m, z_m, r = 0)\,, \\ z_{m+1} &= z(r = \lambda_r | p_m, z_m, r = 0)\,, \end{aligned} \tag{52}$$

which establishes the link between the ray momentum p_m and depth z_m at the distance $r = m\lambda_r$ with their values at $r = (m+1)\lambda_r$, i.e., through the period of perturbation. The phase portrait of the Poincaré map, the so-called Poincaré section, gives a qualitative description of ray motion for various initial conditions. By way of example, consider the canonical Munk USC (14) and the sound speed perturbation in the form

$$\delta c = 2\varepsilon c_0\,\frac{z}{z_{\text{th}}}\,\exp\left(-\frac{2z}{z_{\text{th}}}\right)\sin\frac{2\pi r}{\lambda_r}\,, \tag{53}$$

where $\lambda_r = 10$ km. Such a model approximately describes the effect from the first mode of the internal wave field. In the Poincaré sections, the sets of initial conditions related to nonlinear resonances manifest themselves as chains of ellipsoidal links, and chaotic layers look like disordered clouds of points. Partition of the phase space into regions with regular and chaotic behavior is typical for weakly perturbed Hamiltonian systems. As demonstrated in Fig. 5, with the growth in ε the regions of regular motion shrink, while the chaotic sea broadens because resonance overlapping becomes stronger. The resonances may overlap not fully, but only partially. In this case, the elements of the resonance chain transform into chains of stability islands surrounded by the chaotic sea. For example, Fig. 5c shows the chain of stability islands that corresponds to a partially overlapped 5:1 resonance.

The magnitude of the overlapping parameter K essentially depends not only on the strength of perturbation, but also on the degree of nonlinearity of unperturbed ray oscillations in the waveguide. In particular, it can be shown that

$$K \sim \sqrt{\varepsilon\alpha}\,, \tag{54}$$

i.e., those rays characterized by large values of α become chaotic much more easily. This circumstance served as a rationale to treat the parameter α as the parameter of ray stability [73, 74]. Such a treatment, though, may fail in the

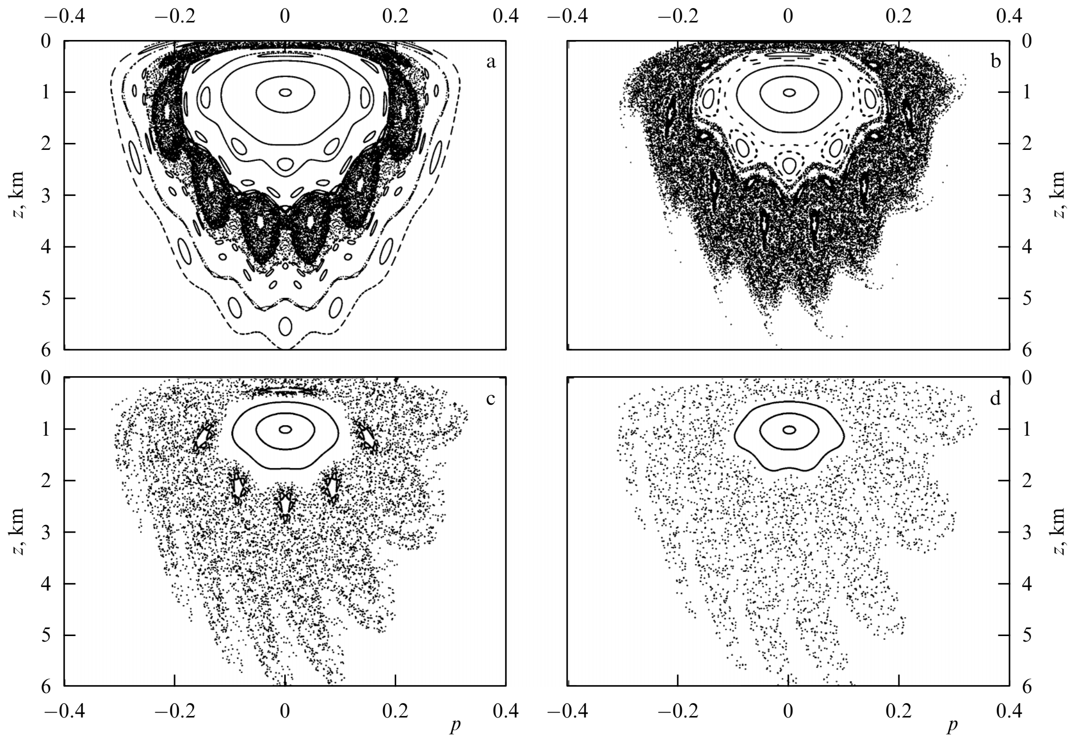

Figure 5. Transformation of the Poincaré section with the increase in amplitude of sound speed perturbations: (a) $\varepsilon = 0.005$, (b) $\varepsilon = 0.01$, (c) $\varepsilon = 0.02$, and (d) $\varepsilon = 0.04$.

presence of strong oscillations of inhomogeneity with respect to depth (see Section 5.2).

If for a certain value of ray action I the derivative $\mathrm{d}\omega/\mathrm{d}I$ and, consequently, the parameter α come to nought, the left inequality in formula (49) does not hold and the above theory of nonlinear resonance becomes inapplicable. This case corresponds to a local degeneracy of the respective Hamiltonian system with the formation of a so-called shearless torus. The ray dynamics in the vicinity of shearless tori are the subject of extensive literature (see the monograph [75] and also articles [76–78]). It is well known that shearless tori demonstrate an extraordinary ability to preserve Lyapunov stability [79]. Moreover, the vanishing of derivative $\mathrm{d}\omega/\mathrm{d}I$ implies a reduced divergence of the nearest rays, which results in the formation of a weakly divergent ray bundle [80–83]. The condition $\mathrm{d}\omega/\mathrm{d}I = 0$ is approximately realized in the USC in the Sea of Japan for rays intersecting the channel axis at approximately 2°. The weakly diverging ray bundle arising in this case can serve as an explanation of the stability of nearly axial rays, which is hinted at by the results of experiments [69, 70]. Analogs of weekly diverging bundles are encountered in quantum mechanics, for example, in describing ferromagnetic spin chains in a magnetic field [84]. We also note that the parameter α is asymptotically connected with the Chuprov waveguide invariant which characterizes temporal and spatial scales of the interference pattern of an acoustic field [85–87].

5.1.2 The influence of nonlinear ray resonance on the characteristics of a wave field. It seems obvious that chaotic ray dynamics should find reflection in the wave picture. In order to clarify this question, we make use of the periodicity of perturbation and introduce the Floquet operator $\hat{F}$ linking the complex-valued field amplitudes at two points on the path, separated by one inhomogeneity period λ_r:

$$\hat{F}u(r,z) = u(r+\lambda_r, z)\,. \tag{55}$$

In quantum mechanics, an analogous operator is applied to describe systems with a perturbation periodic in time. It finds numerous applications in the quantum chaos theory [88].

According to the Floquet theorem, the solution to parabolic equation (7) in a waveguide with a periodic perturbation can be written as a sum of eigenfunctions of operator (55) (referred to as the Floquet modes below):

$$u_m(r,z) = \exp\left(-\frac{\mathrm{i}k\epsilon_m r}{\lambda_r}\right)\Psi_m(r,z)\,, \tag{56}$$

where $\Psi_m(r+\lambda_r, z) = \Psi_m(r,z)$, ϵ_m are some real-valued constants, and $m = 1, 2, \ldots$. The Floquet modes are the mathematical analogs of the Floquet states in quantum mechanics, and quantities ϵ_m are the analogs of quasienergies [23, 88, 89]. Since the Floquet operator is Hermitian, functions $\Psi_m(r,z)$ form a complete orthonormal set. The Floquet modes can be expressed through the modes $\varphi_m(z)$ of unperturbed waveguide. With this goal, consider functions

$$\psi_m(z) \equiv \Psi_m(0,z) \tag{57}$$

and present each of them as the expansion

$$\psi_m(z) = \sum_q C_{qm}\varphi_q(z)\,. \tag{58}$$

In order to find the coefficients C_{qm}, we resort to the matrix representation of the Floquet operator:

$$F_{mn} = \int \mathrm{d}z\,\varphi_m(z)\,\hat{F}\varphi_n(z)\,, \tag{59}$$

where $\hat{F}\varphi_n(z)$ denotes the solution to parabolic equation (7) at $r = \lambda_r$, obtained with the initial condition $u(0,z) = \varphi_n(z)$. The eigenvalues ξ_m and eigenvectors $\mathbf{X}_m$ of the matrix of operator $\hat{F}$, satisfying the equation

$$\hat{F}\mathbf{X}_m = \xi_m\mathbf{X}_m\,, \tag{60}$$

establish the link between the modes of unperturbed waveguide and the Floquet modes. In particular, we have

$$\xi_m = \exp(-\mathrm{i}k\epsilon_m)\,,$$

and the components of the mth eigenvector $\mathbf{X}_m$ are the coefficients of expansion (58) $(C_{1m}, C_{2m}, \ldots)$.

With the help of Floquet modes, we can express the wave field at $r = n\lambda_r$ $(n = 1, 2, 3, \ldots)$ as the expansion

$$u(n\lambda_r, z) = \sum_m g_m(n)\,\psi_m(z)\,, \tag{61}$$

where

$$g_m(n) = \exp(-\mathrm{i}nk\epsilon_m)\,g_m(0)\,. \tag{62}$$

We turn once again to the analogy between the wave and quantum dynamics. It is well known that the action of a periodic perturbation on a quantum system with a discrete spectrum leads to resonance transitions between its energy levels, which obey the relationship

$$\frac{1}{\hbar}\,\Delta E_{m+\Delta m, m} = \omega_{\mathrm{f}}, \tag{63}$$

where $\hbar$ is the Planck constant, $\Delta E_{m+\Delta m, m} = E_{m+\Delta m} - E_m$, E_m is the energy of the mth level, and ω_{f} is the perturbation frequency. A similar phenomenon takes place in periodically inhomogeneous waveguides, too. In this case, a periodic horizontal inhomogeneity gives rise to resonant transfer of acoustic energy between the modes of the unperturbed waveguide. In this case, the resonance condition assumes the form

$$k\Delta E_{m+\Delta m, m} = k_r\,, \tag{64}$$

where $\Delta E_{m+\Delta m, m}$ is the difference between the respective eigenvalues of the Sturm–Liouville problem in the unperturbed waveguide. If the difference $\Delta E_{m+\Delta m, m}$ is small, we can write down that

$$k_r = k\Delta E_{m+\Delta m, m} \simeq \frac{\mathrm{d}E}{\mathrm{d}I}(I_{m+\Delta m} - I_m) = \omega\Delta m\,, \tag{65}$$

where I_m are the action values satisfying quantization rule (29). Thus, Δm coincides with the order of respective nonlinear ray resonance. Moreover, because of the correspondence between rays and modes given by quantization rule (29), the modes of an unperturbed waveguide with the values of action falling in the region of nonlinear ray resonance, viz.

$$k(I_0 - \Delta I_{\max}) + \frac{1}{2} \leqslant m \leqslant k(I_0 + \Delta I_{\max}) + \frac{1}{2}\,, \tag{66}$$

exchange energy most intensively. If the ray resonance is well isolated and does not overlap with its neighbors, the evolution of modes of the unperturbed waveguide that satisfy formula (66) is largely governed by a separate block in the Floquet operator matrix, which is well isolated from the rest of the matrix. Each such block spawns its series of Floquet modes. For overlapping resonances, the respective blocks overlap, too. As a result, inequality (66) becomes violated and the number of effectively interacting modes sharply increases. This phenomenon came to be known in the quantum chaos theory as delocalization [90].

To analyze the relationship between the wave function of a quantum-mechanical system and the structure of phase space of a classical analog of this system, the Wigner function is frequently applied. It is sometimes called the quasiprobability of joint distribution of momentum and coordinate [91]. In the wave theory, the Wigner function of the wave field in the vertical section of the waveguide, $\psi(z)$, defined by the relation

$$W(p,z) = \frac{k}{2\pi}\int \mathrm{d}\zeta\, \psi\left(z-\frac{\zeta}{2}\right)\psi^*\left(z+\frac{\zeta}{2}\right)\exp(\mathrm{i}kp\zeta)\,, \quad (67)$$

is treated as the local spatial field spectrum [43]. Certain important properties of this characteristics of the field become better expressed if one turns to the smoothed Wigner function [91]:

$$w(p,z) = \frac{1}{2\pi\Delta_p\Delta_z}\int \mathrm{d}p'\,\mathrm{d}z'\,W(p',z') \times \exp\left[-\frac{(z-z')^2}{2\Delta_z^2}-\frac{(p-p')^2}{2\Delta_p^2}\right]. \quad (68)$$

If the smoothing scales Δ_p and Δ_z satisfy the condition $\Delta_p\Delta_z = 1/(2k)$, formulas (67) and (68) define the so-called Husimi transform [22]. It is easy to check that, in this case, one obtains

$$w(p,z) = \left|(2\pi\Delta_z^2)^{1/4}\int \mathrm{d}z'\,\psi^*(z')\exp\left[\mathrm{i}kp(z'-z)-\frac{(z'-z)^2}{4\Delta_z^2}\right]\right|^2, \quad (69)$$

where $w(p,z)$ represents the projection of $\psi(z)$ onto the so-called coherent state (the state with minimum uncertainty [45]). The Husimi transform (69) of the eigenfunction $\psi_m(z)$ will be denoted as $w_m(p,z)$.

By way of example, consider functions $w_m(p,z)$ of a waveguide with the reference sound speed profile (14) and periodic perturbation (53) with the amplitude $\varepsilon = 0.01$ and the horizontal period $\lambda_r = 10$ km [43, 89, 92]. The phase portrait of the ray system in this waveguide is displayed in Fig. 6.

Figure 7 exhibits some characteristic Husimi functions of Floquet modes for such a waveguide. All plots show the contours of main islands on the phase portrait. These include the large central island surrounded by five smaller ones formed by the periodic orbits of the 5:1 resonance. Each of the five islands is in turn surrounded by six small satellites. Figure 7 demonstrates that different Floquet modes are localized in different regions of phase space. The modes depicted in Fig. 7a, b, and e are localized inside the stability islands and, consequently, are formed by regular rays. The mode in Fig. 7c, localized near the boundaries of islands of the 5:1 resonance, offers an example of the state that belongs simultaneously to the stable zone and the chaotic sea. States like this correspond to tunneling between the regions of regular and chaotic motion [93]. Such a process is impossible in the classical ray dynamics. In Fig. 7d, the Floquet mode is localized in the vicinity of the unstable periodic ray orbit of the 5:1 resonance. In the Poincaré map, this orbit is represented by five dark circles which are located in Fig. 7e at the maxima of the Husimi function. The localization effect for the Floquet mode in the vicinity of unstable periodic orbit is even more apparent in the field intensity distribution for this mode in the longitudinal waveguide section, i.e., in the $r-z$ plane. In the vicinity of periodic trajectory, one observes an amplified intensity [43, 92]. An analogous phenomenon in the quantum chaos theory is known as scarring [94]. Finally, Fig. 7f plots the Floquet mode belonging to the chaotic sea, i.e., formed by chaotic rays.

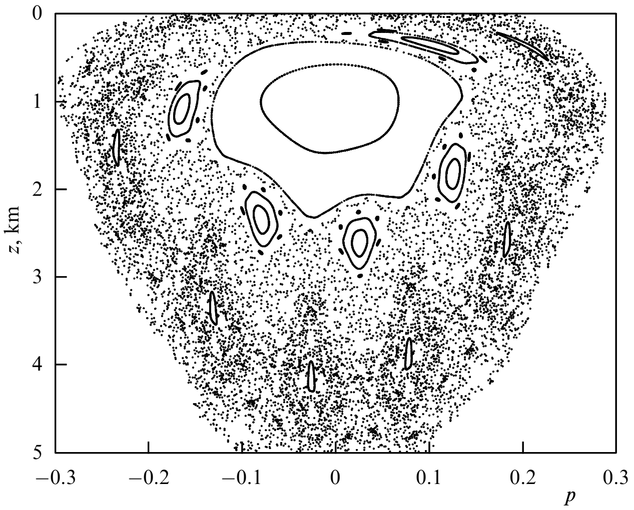

Figure 6. The phase portrait of the ray system in the waveguide model given by the relationships (14) and perturbation (53) with the amplitude $\varepsilon = 0.01$ and the horizontal period $\lambda_r = 10$ km [89].

5.2 Ray dynamics in the presence of fast inhomogeneity oscillations with depth

5.2.1 Vertical resonance. In Section 5.1, we described the mechanism leading to the origin of ray chaos when the sound speed perturbation smoothly depends on the depth z. Here, we continue with a more complex case, when the perturbation exhibits fast oscillations with the depth. In the real ocean such oscillations are caused by high modes of the internal-gravity wave field. As an example, consider a simple model in which the perturbation of the underwater sound channel is described by the formula

$$V(r,z) = \varepsilon Y(z)\sin k_z z \sin k_r r\,, \quad (70)$$

where $Y(z)$ is a slowly varying function, and

$$k_z \gg \left|\frac{\mathrm{d}Y}{\mathrm{d}z}\right|. \quad (71)$$

If this inequality is satisfied, the perturbation exhibits fast oscillations along the ray trajectory, except for the regions

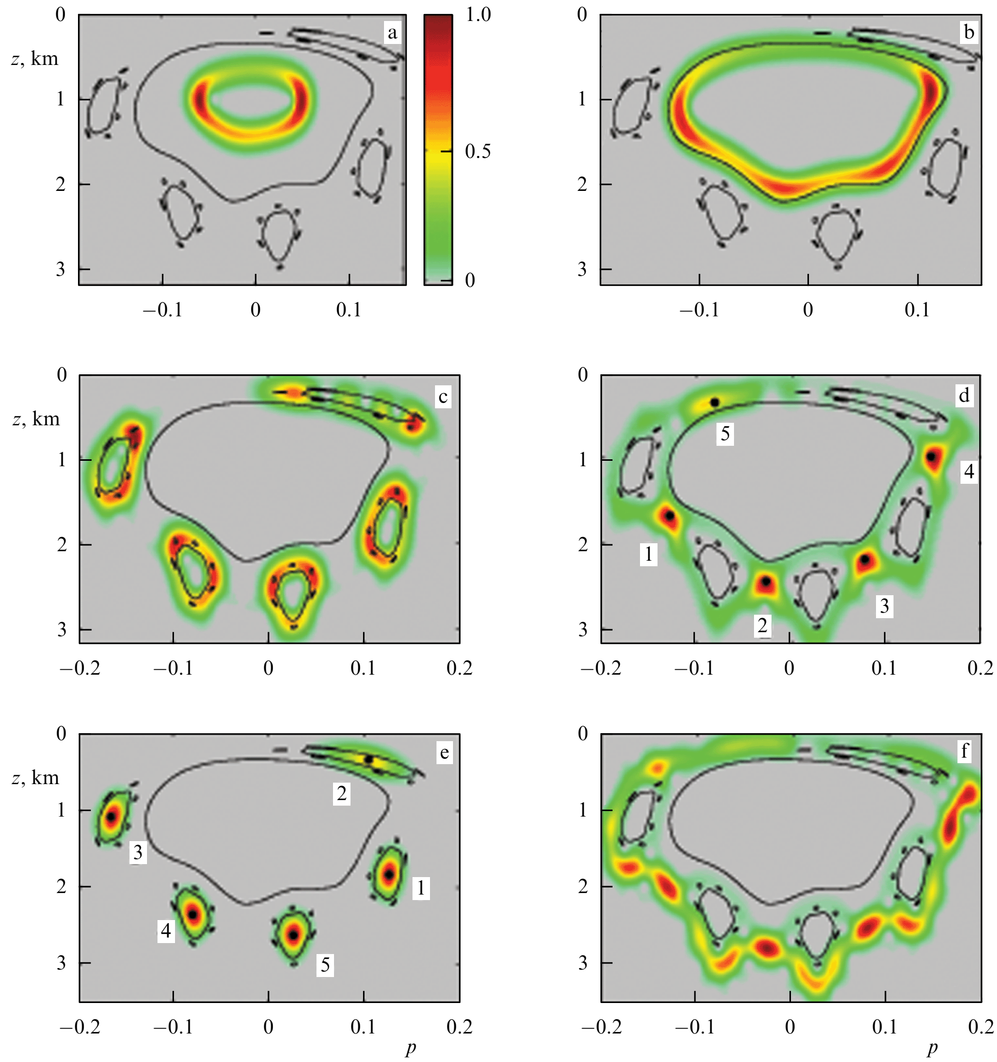

Figure 7. The Husimi functions for different Floquet modes at a frequency of 200 Hz [89]. Solid lines mark the boundaries of islands from the phase portrait of Fig. 6.

satisfying the condition

$$\frac{\mathrm{d}\Psi^{\pm}}{\mathrm{d}r} = k_z p \pm k_r \simeq 0\,, \tag{72}$$

where $\Psi^{\pm} = k_z z \pm k_r r$. In these regions, the oscillations of perturbation become 'frozen' with respect to the ray and the so-called vertical resonance occurs. It is a variety of resonance in systems with fast and slow oscillations explored in detail in a series of studies by A I Neishtadt and colleagues [95–99]. In our case, the role of slow oscillation is performed by the ray oscillations of frequency ω in the waveguide. The approach proposed by Neishtadt's group resides in resolving the motion into resonant and nonresonant components and analyzing each of them subsequently. In the nonresonant mode, the system of ray equations can be reduced to an integrable one with the help of the averaging method [100]. Consider the ray motion in the vicinity of one of the resonances (72), for example, corresponding to $\mathrm{d}\Psi^{+}/\mathrm{d}r = 0$. In this case, the equation for the ray trajectory can be brought into the form

$$\frac{\mathrm{d}^2 z}{\mathrm{d}r^2} = \frac{\mathrm{d}p}{\mathrm{d}r} = -\frac{\mathrm{d}U}{\mathrm{d}z} - \frac{\varepsilon}{2}\, k_z Y(z) \sin \Psi^{+}\,. \tag{73}$$

Using Eqn (73), one readily obtains the system of equations in the Hamiltonian form:

$$\frac{\mathrm{d}\Psi^{+}}{\mathrm{d}r} = k_z y = \frac{\partial \tilde{H}(\Psi^{+}, y)}{\partial y}\,,$$
$$\frac{\mathrm{d}y}{\mathrm{d}r} = -\frac{\varepsilon}{2}\, k_z Y(z) \sin \Psi^{+} - \frac{\mathrm{d}U}{\mathrm{d}z} = -\frac{\partial \tilde{H}(\Psi^{+}, y)}{\partial \Psi}\,, \tag{74}$$

which describes the ray behavior in the vicinity of vertical resonance. Here, y is the deviation from the resonance in terms of the variable p, given by the expression

$$y = p - p_{\mathrm{res}} = p + \frac{k_r}{k_z}\,. \tag{75}$$

The resonance Hamiltonian $\tilde{H}$, in accordance with equations (74), has the following form

$$\tilde{H}(\Psi^{+}, y) = \frac{k_z y^2}{2} - \frac{\varepsilon}{2}\, k_z Y \cos \Psi^{+} + \frac{\mathrm{d}U}{\mathrm{d}z}\, \Psi^{+}\,. \tag{76}$$

Subject to the inequality

$$\left|\frac{\mathrm{d}U}{\mathrm{d}z}\right| < \frac{\varepsilon k_z Y}{2}\,, \tag{77}$$

the phase portrait of a system of equations (74) for the fixed value of z contains the region of oscillatory motion bounded by a separatrix, the region corresponding to the vertical resonance. The area of this region depends on z and varies along the ray. Rays, therefore, can intersect the separatrix, getting into the separatrix loop and, accordingly, into the vertical resonance. The criterion of getting into the vertical resonance can be formulated as the inequality [101]

$$\tilde{H}\Big|_{z(r)} \leqslant \tilde{H}_{\mathrm{s}}\Big|_{z(r)}\,, \tag{78}$$

where H_{s} is the value of Hamiltonian $\tilde{H}$ on the separatrix, the values of phase Ψ^{+} are bounded within the interval $[-\pi, \pi]$, and the index $z(r)$ implies that $\tilde{H}$ and $\tilde{H}_{\mathrm{s}}$ are computed along the ray trajectory $z(r)$. The area of resonance region reaches a maximum at $\mathrm{d}U/\mathrm{d}z = 0$, i.e., when the ray crosses the axis of the USC. In this case, one expects the influence of a vertical resonance to be the strongest. Taking this into account together with condition (72), we find the equation defining the rays most susceptible to the influence of the vertical resonance [102, 103]:

$$p(z_{\mathrm{a}}, H) = \sqrt{2\big[H - U(z_{\mathrm{a}})\big]} \simeq \frac{k_r}{k_z}\,, \tag{79}$$

where z_{a} is the depth of the channel axis.

Having been trapped in the vertical resonance, the ray leaves it later, since inequality (77) can hold only along a limited portion of the trajectory. Every passage of the ray through the vertical resonance results in a jump in the ray action I. As proved in Refs [95, 96], the magnitude of this jump is extremely sensitive to the initial conditions. As a result, multiple transits through the resonance give birth to chaotic diffusion. Moreover, Neishtadt and Vasiliev [104] have proven the absence of stable periodic trajectories among those intersecting the separatrix of the resonance domain.

Thus, ray scattering on the vertical resonance spawns ray chaos. In this case, Eqn (79) defines the position of the chaotic layer in the phase space. For example, in the case of strong vertical oscillations, $k_r \ll k_z$, the vertical resonance leads to chaos for the rays propagating at small angles to the channel axis and belonging to the central domain of the phase space. This is demonstrated in Fig. 8 which plots the Poincaré section computed for a USC with a biexponential sound speed profile:

$$c(z) = c_0\left\{1 + \frac{b^2}{2}\left[\exp\left(-az\right) - \eta\right]^2\right\}, \tag{80}$$

where $c_0 = 1480$ m s^{-1}, $a = 0.5$ km^{-1}, $b = 0.557$, and $\eta = 0.6065$. The perturbation has the form (70), where

$$Y(z) = \frac{z}{z_{\mathrm{th}}}\exp\left(-\frac{2z}{z_{\mathrm{th}}}\right). \tag{81}$$

The values of the perturbation parameters are the following: $z_{\mathrm{th}} = 1$ km, $\varepsilon = 0.005$, $k_z = 2\pi/0.2$ km^{-1}, and $k_r = 2\pi/5.0$ km^{-1}. As is seen from the depicted Poincaré section, rays traveling at small angles to the channel axis belong to the extended chaotic sea. This helps to explain on a qualitative level the characteristic features of received acoustic signals in a series of experiments on long-range sound propagation [19, 66]. First, the near-axial rays are characterized by the slowest propagation velocities. Accordingly, scattering on the vertical resonance can be an explanation for strong spreading and irregularity of the tail part of the acoustic signal. Second, as mentioned above, the dynamics of rays that escape the vertical resonance can be reduced to the integrable dynamics by averaging over fast phases $\Psi^{\pm}$. Such rays are therefore exhibit Lyapunov stability. This offers a key to understanding the stability of early signal arrivals formed by relatively steep rays. Hence, it also follows that early arrivals can certainly be used for solving hydroacoustic tomography tasks.

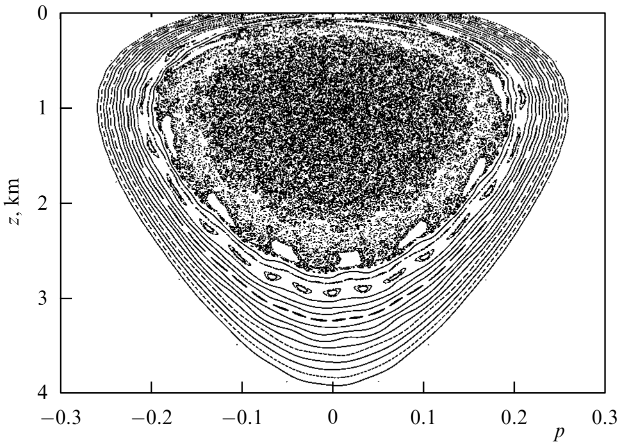

Figure 8. The Poincaré section for a USC with a biexponential sound speed profile and the perturbation (70).

5.2.2 Bifurcations of periodic orbits. The theory of vertical resonance treats ray dynamics at a somewhat different angle than the nonlinear resonance theory considered in Section 5.1. We would like to learn how these two approaches are related [43, 105]. With this goal, we consider the Hamiltonian

$$H = H_0(I) + \varepsilon F(I, \vartheta, r)\sin\big(k_z z(I, \vartheta)\big) \tag{82}$$

with a periodic perturbation $F(I, \vartheta, r) = F(I, \vartheta, r + \lambda_r)$. Let us assume that the function F includes many horizontal harmonics. Condition (79) then takes the form

$$p_{\max}^{(m)} = \frac{mk_r}{k_z}\,, \tag{83}$$

where m is the order of a harmonic. Consider a certain nonlinear resonance

$$l\omega = mk_r = \frac{2\pi m}{\lambda_r}\,. \tag{84}$$

The resonant Fourier amplitude of the perturbation is computed in the following way:

$$H_{l,m} = \frac{1}{8\pi\mathrm{i}\lambda_r}\int_{-\lambda_r/2}^{\lambda_r/2}\mathrm{d}r\,\exp\left(-\mathrm{i}\,\frac{2\pi mr}{\lambda_r}\right)W_l(I, r) + \text{c.c.}, \tag{85}$$

$$W_l(I, r) = \int_{-\pi}^{\pi}\mathrm{d}\vartheta\,F(I, \vartheta, r)\exp\left(-\mathrm{i}l\vartheta + \mathrm{i}k_z z\right) - \int_{-\pi}^{\pi}\mathrm{d}\vartheta\,F(I, \vartheta, r)\exp\left(-\mathrm{i}l\vartheta - \mathrm{i}k_z z\right). \tag{86}$$

For large k_z, the integrals on the right-hand side of Eqn (86) can be computed with the help of the stationary phase method. Let us introduce the notation

$$\Psi_{1,2} = -l\vartheta \pm k_z z(\vartheta)\,, \tag{87}$$

in which case the conditions that the phase be stationary become the following:

$$\frac{\mathrm{d}\Psi_{1,2}}{\mathrm{d}\vartheta} = -l \pm k_z\,\frac{\mathrm{d}z}{\mathrm{d}\vartheta} = -l \pm \frac{k_z p}{\omega} = 0\,. \tag{88}$$

According to formulas (84), the frequency ω can be replaced by the quantity mk_r/l, and we obtain

$$mk_r \pm k_z\,p(I,\vartheta) = 0\,. \tag{89}$$

The contribution of stationary phase points depends on the second derivative

$$\frac{\mathrm{d}^2\Psi_{1,2}}{\mathrm{d}\vartheta^2} = \pm\frac{k_z}{\omega^2}\,\frac{\mathrm{d}p}{\mathrm{d}r}\,. \tag{90}$$

Making use of the approximation

$$\frac{\mathrm{d}p}{\mathrm{d}r} \approx -\frac{\mathrm{d}U}{\mathrm{d}z}\,, \tag{91}$$

and performing integration in Eqn (86), we find

$$W(I,r) \approx \frac{1}{2\mathrm{i}}\sum_j\left(D\sqrt{k_z\left|\frac{\mathrm{d}U}{\mathrm{d}z}\right|}\,\right)^{-1} F(\vartheta_j, r) \times \exp\left(\mathrm{i}\Psi_j + \mathrm{i}\,\frac{\pi}{4}\,\mathrm{sgn}\,\frac{\mathrm{d}\Psi_j^2}{\mathrm{d}\vartheta^2}\right) + \text{c.c.}, \tag{92}$$

where the index l is omitted, ϑ_j is the jth solution to equation (89) in ϑ, and Ψ_j takes the values Ψ_1 or Ψ_2 that corresponds to it. From Eqn (92) it follows that the function $H_{l,m}(I)$ has singularity if $\mathrm{d}U/\mathrm{d}z = 0$ and $|p| = p_{\mathrm{res}}$. Comparing this with Eqn (89), we find that the singularity occurs when the vertical resonance condition (83) holds true. Hence, it follows that nonlinear resonances residing in close proximity to the zone of vertical resonance in phase space experience substantial broadening. This results in locally enhanced resonance overlapping and the appearance of an extended chaotic layer. On the other hand, nonlinear resonances located far from the vertical resonance zone turn out to be suppressed since the values of respective Fourier amplitudes are close to zero because of strong oscillations of the integrand in Eqn (86).

However, the case considered here admits a much more interesting scenario for the origin of chaos. A selective amplification of Fourier amplitudes may result in increasing the derivatives $\mathrm{d}H_{l,m}/\mathrm{d}I$ and $\mathrm{d}^2H_{l,m}/\mathrm{d}I^2$. The ensuing consequences can be illustrated in the following way. Take equation (45b), and rewrite it in the form

$$\frac{\mathrm{d}\vartheta}{\mathrm{d}r} = \frac{\partial H_0(I)}{\partial I} + \varepsilon\,\frac{\partial H_{l,m}(I)}{\partial I}\cos\Psi_{l,m}\,, \tag{93}$$

where $\Psi_{l,m} = l\vartheta - mk_r r + \phi_0$. Consider the properties of equation (93) in the vicinity of elliptic ray orbits of nonlinear resonance, satisfying the conditions $\Psi_{l,m} = 0$ and $l\,\mathrm{d}\vartheta/\mathrm{d}r = mk_r$. In this case, equation (93) transforms into

$$\frac{m}{l}\,k_r = \frac{\partial H_0(I)}{\partial I} + \varepsilon\,\frac{\partial H_{l,m}(I)}{\partial I}\,. \tag{94}$$

If the inequality

$$\left|\frac{\partial^2 H_0}{\partial I^2}\right| > \varepsilon\left|\frac{\partial^2 H_{l,m}}{\partial I^2}\right| \tag{95}$$

is satisfied, equation (94) has a single root defining the action variable that corresponds to the elliptic point. In the presence of vertical resonance, however, this inequality becomes violated already for small amplitudes of perturbation ε. In this case, two additional roots may appear, each corresponding to a periodic ray orbit, either elliptic or hyperbolic. Thus, bifurcation of one of two types takes place: either pitchfork or saddle–center. An analogous situation is encountered for hyperbolic ray orbits that correspond to the conditions $\Psi_{l,m} = \pi$ and $l\,\mathrm{d}\vartheta/\mathrm{d}r = mk_r$. Bifurcations of elliptic and hyperbolic orbits happen for nearly the same values of ε. New elliptic orbits appearing as the result of bifurcation may correspond to new island chains in the phase space. In this case, the nonlinear resonance of multiplicity $l{:}m$ gains two satellites. The reproduction of periodic ray orbits accompanies a further increase in ε.

As an illustration, let us follow the inception of the chaotic layer plotted in Fig. 8 for small values of the perturbation amplitude ε. Figure 9 illustrates the evolution of the Poincaré section with a growth in ε. The vertical resonance with $p_{\max} = 0.04$ leads to broadening of the nonlinear 15:2 resonance. As a result, this resonance becomes apparent in the Poincaré section even for a very small ε. At $\varepsilon = 0.0001$, the island chain that corresponds to the 15:2 resonance looks like a usual resonance chain in nondegenerate Hamiltonian systems (Fig. 9a). At $\varepsilon = 0.0002$, this is already not the case — the islands elongate along the radial coordinate (Fig. 9b). This stretching leads in the end to bifurcations of singular points. The result of bifurcations is displayed in Fig. 9c, where we observe the appearance of two chain-satellites with the same number of islands. Thus, the nonlinear 15:2 resonance turns out to be triply degenerate. As ε grows even further, a chaotic layer forms in the place of separatrices of degenerate resonances. This example confirms that chaos in the presence of vertical resonance can evolve according to the scenario characteristic of degenerate Hamiltonian systems [75–79, 106].

5.2.3 The influence of vertical resonance on wave field properties. The applicability of the ray method relies on the smallness of the acoustic wavelength, as compared with inhomogeneity scales of the ocean. The ocean is a stratified medium, and its horizontal variability scale L_r exceeds its vertical scale by two or three orders of magnitude, namely

$$L_z \ll L_r\,. \tag{96}$$

On the other hand, the wave vector of an acoustic wave also has two components, vertical and horizontal. A USC is capable of confining only the waves propagating at small angles to the horizontal plane; hence, the vertical wave number is much less than the horizontal one. It thus follows that the vertical length of an acoustic wave can be of the same order as L_z. In that case, the ray approximation will incorrectly describe the influence of vertical inhomogeneity on the wave propagation [107].

Reference [108] reports that small-scale structures of the sound speed profile do not exert a strong influence on the sound wave refraction, and that the accuracy of ray modeling

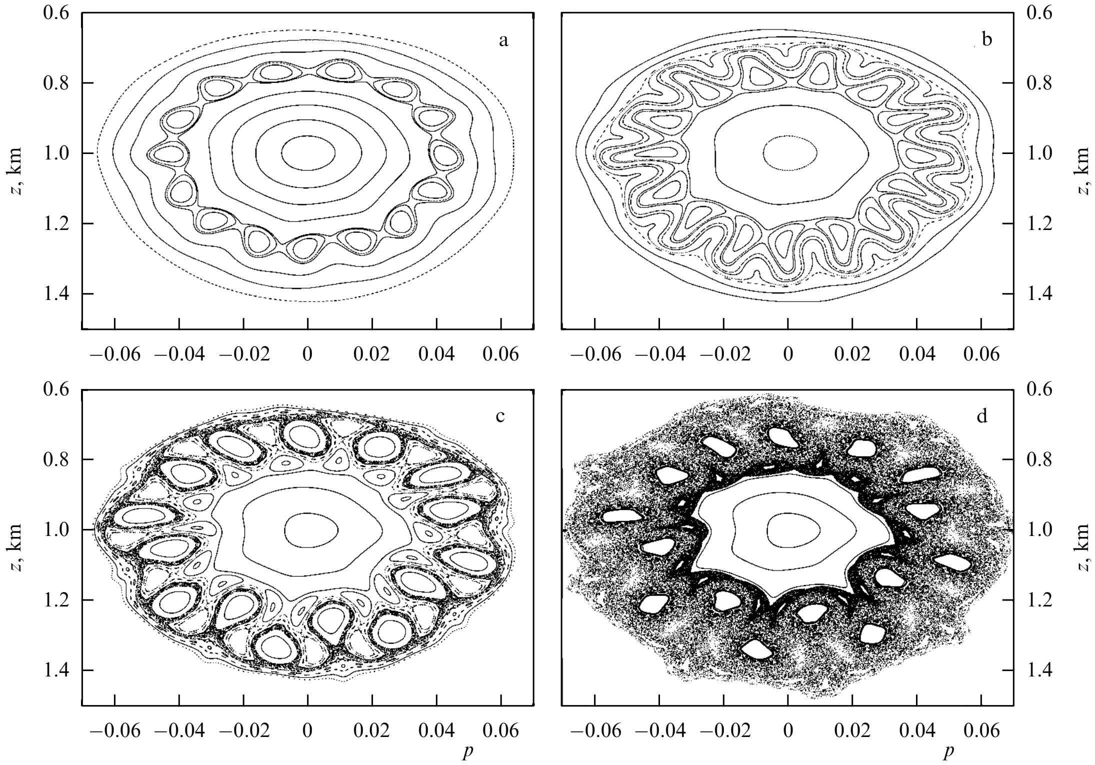

Figure 9. Formation of a chaotic layer in the vicinity of vertical resonance at $\lambda_z = 0.2$ km and $\lambda_r = 5$ km: (a) $\varepsilon = 0.0001$, (b) $\varepsilon = 0.0002$, (c) $\varepsilon = 0.00035$, and (d) $\varepsilon = 0.0005$.

can substantially be improved by smoothing the perturbed sound speed profile. Smoothing, however, removes small-scale depth variations of perturbation, which play a key role in the stochastization of near-axial rays. This hints that wave effects must suppress the influence of vertical resonance on the near-axial sound propagation.

In order to test the last statement, we turn to the properties of the Floquet modes for the USC model corresponding to Fig. 8. Figure 10 demonstrates the Husimi distributions for two typical Floquet modes at a sound frequency of 200 Hz. A part of the Floquet modes is 'stretched' in the phase space, similarly to the mode plotted in Fig. 10a, covering almost entirely the chaotic sea. To what extent do such Floquet modes correspond to the instability of sound propagation at small angles to the USC axis? Reference [109] shows with the help of the Leboeuf–Voros criterion [110] that these Floquet modes can only be classified as 'weakly chaotic'. Reference [111] explores the dynamics of a wave packet in the phase space with the help of the Husimi function (69). It indicates that at a frequency of 200 Hz (and lower) the phase volume occupied by the wave packet oscillates instead of growing monotonically with an increase in the horizontal coordinate r, as prescribed by the theory of ray chaos.

We would like to focus our attention on the following phenomenon. Many of the Floquet modes belonging to the chaotic sea look like chains of eight ordered intense spots (Fig. 10b). Each such burst is located in the vicinity of one of the periodic orbits of a 8:1 resonance. All these orbits are unstable, which allows one to connect the spot formation with scarring, i.e., the wave functions localized in the vicinity of unstable periodic orbits [94].

On the other hand, as shown in Section 5.2.2, under the conditions of vertical resonance the number of periodic orbits can sharply increase as a result of a bifurcation cascade. Indeed, direct computation of periodic ray orbits with the length $8\lambda_r$, which may correspond to a chain of eight intensity bursts, gives an immense number of solutions, with the initial points of the orbits being scattered without order in phase space (Fig. 10c). If we take into account that the contribution of an orbit is inversely proportional to the rate of its Lyapunov divergence, the situation is partly clarified: the eight of nine most stable orbits are located in the vicinity of elliptic points of the 8:1 resonance (Fig. 10d).

It should be noted that a cluster formed by several less stable orbits is present in the vicinity of each of these eight orbits. If the sound frequency is insufficiently high, the contributions of separate orbits belonging to the same cluster are indistinguishable. As a result, the clusters are reflected in the Floquet modes as *superscars* — spots of high intensity concomitant to orbit bifurcations [113]. As the frequency of sound is reduced, the traces of periodic orbit bifurcations in the structure of Floquet modes become weaker and weaker, before fading away altogether [103, 109, 111].

5.3 Ray and wave chaos in randomly inhomogeneous waveguides: the quasideterministic approach

The methods and approaches used to explore deterministic periodic waveguides differ essentially from those of the theory of waves in random media. One of the most important properties of periodic waveguides, influencing many aspects of both ray and wave dynamics, is the sharp separation of the phase space of ray equations into regular and chaotic domains. The ray motion is regular and predictable within the former, and exhibits stochastic properties within the latter. This, undoubtedly, leaves imprints on the properties of acoustic fields when correspondence conditions between the ray and wave descriptions are fulfilled.

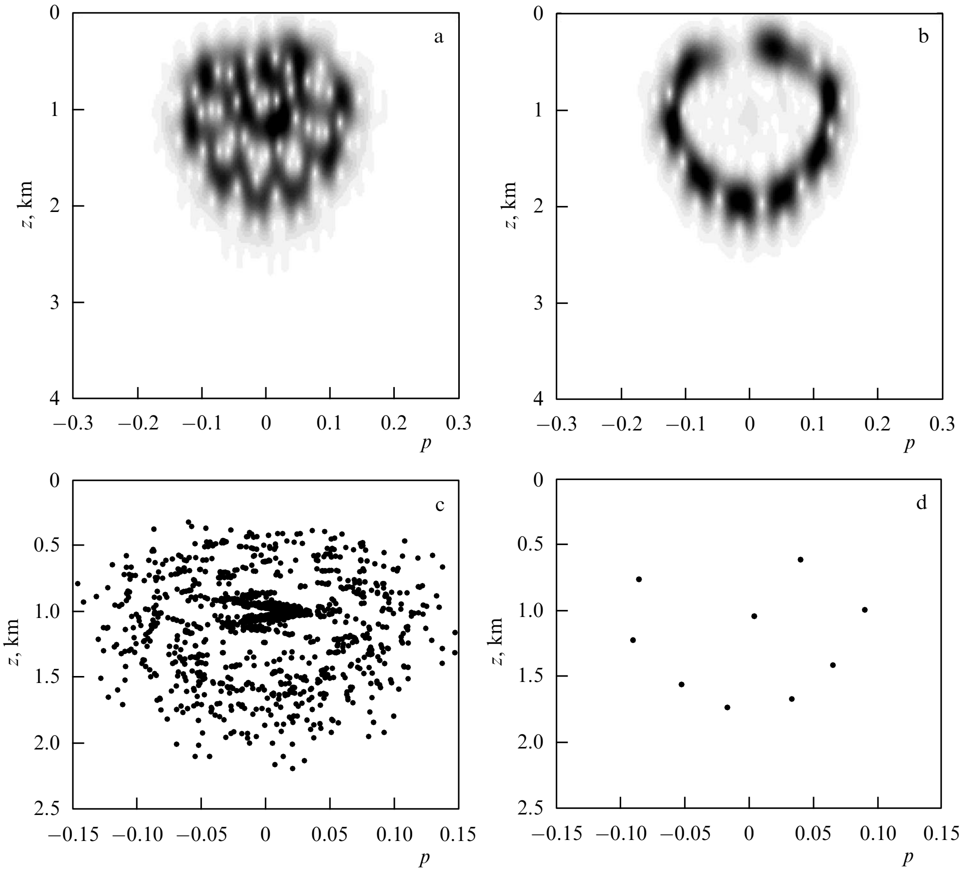

Figure 10. (a) An example of the Husimi distribution for the Floquet mode covering the chaotic layer. (b) The Husimi distribution for the Floquet mode localized in the vicinity of periodic orbits of the 8:1 resonance. (c) Localization of orbits with period $8\lambda_r$ in phase space. (d) The most stable of such orbits [112].

Notions of the Lyapunov ray instability and the predictability horizon are also applicable to waveguides with random perturbations. In this case, one assumes the ergodicity of ray dynamics in phase space, which is rather natural since the broad spectrum of perturbation harmonics leaves no chance for the existence of impermeable stability zones. At the same time, studies of the statistics of the Lyapunov exponents at a finite distance from the source reveal that a considerable fraction of rays preserves stability over distances essentially exceeding the Lyapunov horizon [18]

$$r_{\mathrm{Lyap}} = \frac{1}{\nu}\,, \tag{97}$$

where ν is the global Lyapunov exponent (i.e., the exponent as $r \to \infty$).

Such rays form compact beams which can stand out through their intensity owing to the reduced geometrical divergence. Reference [31] dubbed them 'coherent clusters'. One has to distinguish coherent clusters from regions of random field focusing responsible for the formation of caustics [114, 115]. The main difference lies in the fact that the initial conditions for rays belonging to a coherent cluster form a compact set in phase space, the position of which may change depending on realizations of random inhomogeneities. A set of this kind can be singled out by different techniques, for example, by computing the map of stability exponents in the phase space or with the assistance of computations of eigenfunctions for the Frobenius–Perron operator [116]. For a perturbation composed of a small number of harmonics, use can be made of the method proposed in Ref. [117].

If our goal is not only to find coherent clusters, but also to propose some physical explanation for their formation, we can resort to the one-step Poincaré map method [118–120] based on a reduction in ray propagation on a limited path in a randomly inhomogeneous waveguide to the equivalent quasi-deterministic problem with a periodic inhomogeneity. Below, we give a brief description of this method.

Consider the ray Hamiltonian of the following form

$$H = \frac{p^2}{2} + U(z) + \varepsilon Y(z)\,\xi(r,z)\,, \tag{98}$$

where $\varepsilon \ll 1$, $Y(z)$ is a slowly varying function, and $\xi(r,z)$ is the random function satisfying the conditions

$$\langle \xi(r,z) \rangle = 0\,, \quad \langle \xi^2(r,z) \rangle = \frac{1}{2}\,. \tag{99}$$

Suppose that $\xi(r,z)$ is a differentiable function with known spectral properties and consider some its realization. This allows us to treat $\xi(r,z)$ as an unknown deterministic function. In order to identify the regions of initial conditions corresponding to coherent clusters, we make use of the invariance condition on a finite interval: if some set of initial conditions in phase space transforms into itself without mixing at $r = \tau$, it corresponds to Lyapunov stable trajectories in the interval $r \in [0, \tau]$. Such sets can be found with the help of the map

$$p_{i+1} = p(r = \tau | p_i, z_i, r = 0)\,, \qquad z_{i+1} = z(r = \tau | p_i, z_i, r = 0)\,, \tag{100}$$

where $p(r = \tau | p_i, z_i, r = 0)$ and $z(r = \tau | p_i, z_i, r = 0)$ are the solutions to ray equations at $r = \tau$ that correspond to the initial conditions $p(r = 0) = p_i$ and $z(r = 0) = z_i$. We stress that all map iterations are carried out with the help of one and the same 'piece' of the function $\xi(r, z)$. Hence, it follows that map (100) is equivalent to an ordinary Poincaré map for Hamiltonian (98) in which the function $\xi(r, z)$ is replaced by the periodic function $\tilde{\xi}$:

$$\tilde{\xi}(r' + n\tau, z) = \xi(r', z)\,, \quad 0 \leqslant r' \leqslant \tau\,, \tag{101}$$

where $n = 0, 1, 2, \ldots$. The main distinction of map (100) from the ordinary Poincaré section lies in the fact that map (100) describes the dynamics only within the finite interval $r \in [0, \tau]$, whereas the range of values for r is not bounded for the ordinary Poincaré map. Relatedly, map (100) came to be known as the one-step Poincaré map.

The main property of the one-step Poincaré map stems from the analogy with the ordinary Poincaré map: *each point of continuous closed trajectory of the one-step Poincaré map* (100) *corresponds to the initial condition for the trajectory of a ray which preserves Lyapunov stability in the interval* $r \in [0, \tau]$. Note that the inverse statement is generally incorrect; therefore, the given stability condition is not a necessary one.

The main advantage of the one-step Poincaré map is that it admits a qualitative analysis with the help of the theory of periodic waveguides. As an illustration, consider the simplest case when ξ does not depend on the depth z. Then, in accordance with conclusions of Section 5.1, the structure of the phase portrait of map (100) is governed by the nonlinear resonances

$$l\omega(I) = mk_r\,, \tag{102}$$

where $k_r = 2\pi/\tau$. For $\tau \ll 2\pi/\omega$, the impact of resonances can be neglected, since the corresponding Fourier amplitudes are small, and the system of ray equations can be reduced to the integrable one with the help of the averaging method. Thus, the rays become chaotic only gradually. Of interest is the case of large values of $\tau \gg 2\pi/\omega$. Since the function $\tilde{\xi}(r)$ contains an infinite number of harmonics, an infinite number of $n \times l : n \times m$ resonances, where n is an integer number, correspond to each resonance value of action satisfying relation (102). Realizing that the amplitudes of resonances decay quite fast with a growth in their order, we can neglect all resonances with $|n| > 1$. In that case, one readily obtains the expression for the resonance width with respect to the spatial frequency of ray oscillations in the waveguide:

$$\Delta\omega = 2\sqrt{\varepsilon|\omega' Y_l\, \xi_m|}\,, \tag{103}$$

where Y_l and ξ_m are the resonance amplitudes of the Fourier series for the functions $Y(\vartheta)$ and $\tilde{\xi}(r)$. It is noteworthy that as τ grows the fluctuations of quantity ξ_m weaken and $\xi_m \to \text{const} \times S(v = k_r)$, where $S(v)$ is the spectral density for the function $\xi(r)$. Thus, for large τ the resonance widths rather weakly depend on realizations of random perturbation. The Fourier amplitudes Y_l also decay quite fast with increasing l. We may therefore limit ourselves to considering only the resonances with $l = 1$. In this case, the distance between the nearest resonances in terms of frequency is described by the simple formula

$$\delta\omega = \frac{2\pi}{\tau}\,. \tag{104}$$

Making use of the Chirikov criterion

$$K = \frac{\Delta\omega(\tau)}{\delta\omega(\tau)} \simeq 1\,, \tag{105}$$

we can estimate the minimum distance from the sound source up to which the ray dynamics is predominantly Lyapunov stable.

Let us turn now from the ray to the wave description. In this case, the role of the one-step Poincaré map is played by the shift operator [121]

$$\hat{G}u(r = 0, z) = u(r = \tau, z) \tag{106}$$

describing the wave field evolution between $r = 0$ and $r = \tau$. In the same manner, as the one-step Poincaré map is an analog of the ordinary Poincaré map, the operator $\hat{G}$ is the analog of the Floquet operator (55). Eigenfunctions and eigenvalues of the operator $\hat{G}$ are defined by the relationship

$$\hat{G}u_m(r, z) = \exp(-\mathrm{i}k\epsilon_m)\, u_m(r, z)\,. \tag{107}$$

Similarly to the Floquet operator, the operator $\hat{G}$ can be expanded over the basis of the modes of an unperturbed waveguide with the help of representation (59). The connection between stability (instability) of rays and wave dynamics can be judged both by the structure of separate wave functions, as we did earlier in Section 5.1, and by the statistical properties of the spectrum. In the quantum chaos theory, one of the most representative characteristics, which points to the degree of manifestation of classical chaos in quantum dynamics, is the distribution of level spacings defined as

$$s = \epsilon_{m+1} - \epsilon_m\,. \tag{108}$$

As applied to the operator $\hat{G}$, it is reasonable to use the distribution of level spacings, which is averaged over the ensemble of realizations of random inhomogeneity:

$$\rho(s, \tau) = \lim_{N\to\infty} \frac{1}{N} \sum_{n=1}^{N} P_n(s, \tau)\,, \tag{109}$$

where $P_n(s, \tau)$ is the distribution of level spacings computed with the nth inhomogeneity realization. The regular ray dynamics implies that the modes tend to combine in separate groups which weakly interact with each other. As a result, in accordance with the theory of random matrices, the matrix of operator $\hat{G}$ attains a block structure, each block giving birth to its own series of eigenvalues ϵ_m. Moreover, the series of eigenvalues spawned by different matrix blocks do not correlate with each other. Accordingly, the statistics of level spacings s is described by the Poisson distribution [88, 122]

$$\rho(s) \sim \exp(-s)\,. \tag{110}$$

The global ergodic chaos assumes a dissimilar picture — all modes strongly interact with each other, while the wave functions overlap in the phase space. In this case, the nearest levels experience 'repulsion' and the level spacings are

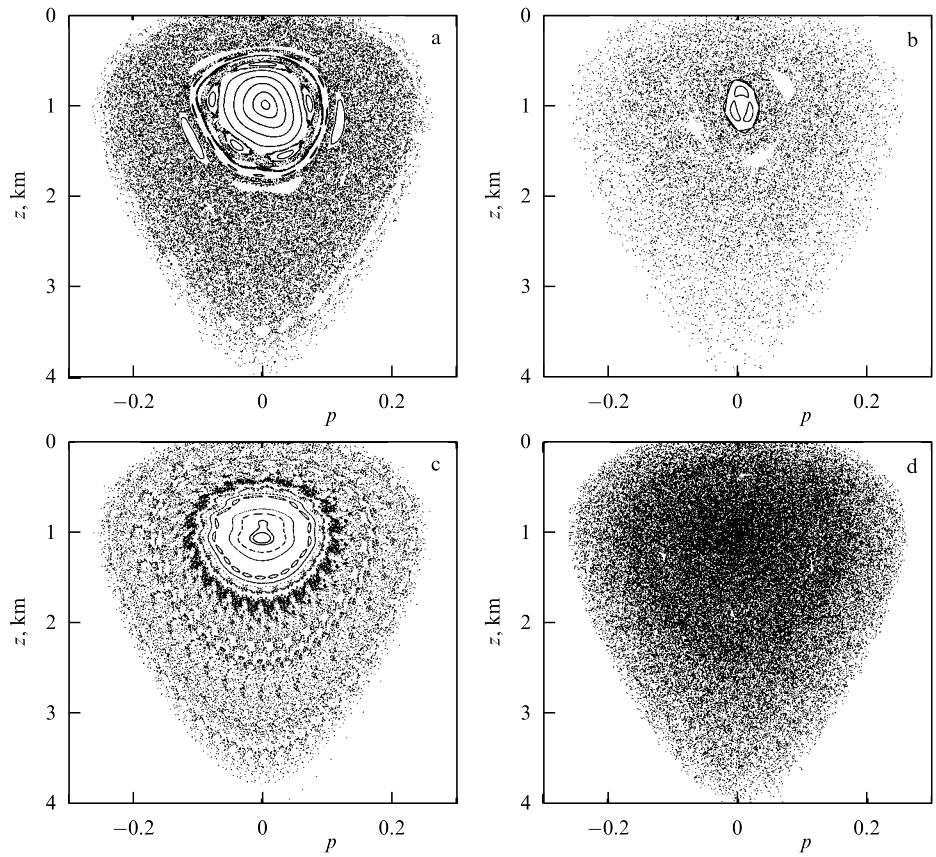

Figure 11. Examples of phase portraits constructed with the help of map (100) for a USC with a biexponential sound speed profile and the perturbation (115). Parameter values are as follows: (a) $v = 5$, $\tau = 100$ km, (b) $v = 5$, $\tau = 500$ km, (c) $v = 20$, $\tau = 10$ km, and (d) $v = 20$, $\tau = 30$ km.

distributed according to the Wigner–Dyson law [88, 122]

$$\rho(s) = As^{\zeta} \exp(-Bs^2)\,, \tag{111}$$

where A and B are the constants selected so as to satisfy the normalization conditions

$$\int_0^{\infty} \rho(s)\,\mathrm{d}s = 1\,, \qquad \int_0^{\infty} s\rho(s)\,\mathrm{d}s = 1\,, \tag{112}$$

and ζ takes the values of 1, 2, or 4, depending on the symmetry of the operator $\hat{G}$. The eigenvalues of operator $\hat{G}$ are unimodular (i.e., they lie on the unit circle in the complex plane), while the operator $\hat{G}$ itself does not generally possess symmetry with respect to inversion of the horizontal coordinate r. These two circumstances indicate that the operator $\hat{G}$ belongs to a circular unitary ensemble for which $\zeta = 2$ [121]. An intermediate regime of a mixed phase space which hosts regions of regular and chaotic ray dynamics corresponds to a certain combination of the Poisson and Wigner–Dyson statistics. Finding a satisfactory expression for $P(s)$ in this case is rather difficult [123, 124]. In practice, one frequently uses the approximation of statistics of interlevel separations based on the heuristic Brody distribution [88, 125]

$$\rho(s) = (\beta + 1)A_{\beta} s^{\beta} \exp(-A_{\beta} s^{\beta+1})\,, \tag{113}$$

where

$$A_{\beta} = \left[\Gamma\left(\frac{\beta+2}{\beta+1}\right)\right]^{\beta+1}, \tag{114}$$

and $\Gamma(\ldots)$ is the Euler gamma-function. At $\beta = 0$, formula (113) reduces to the Poisson distribution, and for $\beta = 1$ to the Wigner distribution (i.e., the Wigner–Dyson distribution with $\zeta = 1$). As the step τ increases, the net area of stability regions of map (100) decreases, while the area of chaotic regions increases. The distinction between the Wigner–Dyson distributions for $\zeta = 1$ and $\zeta = 2$ is quite small. Taking this into account, it should be expected that the value of the Brody parameter β that corresponds to the best approximation will vary with the growth of τ from 0 to 1, reflecting the origin of chaos.

In order to check this assumption, consider a USC with a biexponential sound speed profile (80) and the perturbation

$$\begin{aligned} \delta c(r,z) &= \varepsilon c_0 \frac{z}{z_{\mathrm{th}}} \exp\left(-\frac{2z}{z_{\mathrm{th}}}\right) \sin\gamma(r,z)\,\mu(r)\,, \\ \gamma(r,z) &= \pi\left(v \exp\left(-\frac{z}{z_{\mathrm{th}}}\right) + \mu(r)\right). \end{aligned} \tag{115}$$

Here, $\varepsilon = 0.0014$, and $z_{\mathrm{th}} = 1$ km. The function $\mu(r)$ represents the sum of 10,000 harmonics with random phases and wave numbers k_r distributed over the interval from $2\pi/100$ km^{-1} to 2π km^{-1} with the spectral density decaying as k_r^{-2}. The function $\mu(r)$ is constrained by the normalization condition $\langle \mu^2 \rangle = 1$. Figure 11 demonstrates examples of ray phase portraits of map (100). At $v = 5$, the perturbation oscillates with depth sufficiently gently, and the ray chaos develops with the growth of τ according to the scenario that corresponds to overlapping resonances. The

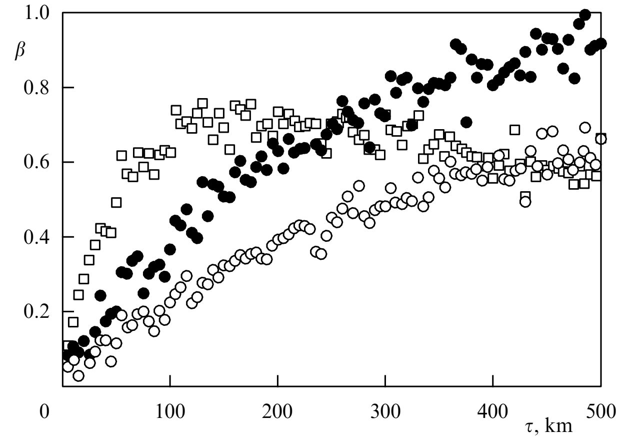

Figure 12. The Brody parameters β as a function of τ. The white circles correspond to $f = 200$ Hz and $v = 5$; the black circles are consistent with $f = 200$ Hz and $v = 20$, and the squares are peculiar to $f = 600$ Hz and $v = 20$.

area of the regular motion region slowly decreases as τ increases, so that a small stability island is preserved even at distances in excess of several hundred kilometers from the source. In the case of $v = 20$, the vertical oscillations of perturbation are strong. Relatedly, chaos develops according to the scenario presented in Section 5.2. In this case, all stability regions disappear quite fast, and they are already absent at $\tau = 30$ km.

The dependence of the Brody parameter on τ at the frequency of 200 Hz, plotted in Fig. 12, corresponds to our expectations on the whole: β increases, on average, with the growth in τ, and this growth is faster for $v = 20$ than for $v = 5$. We should, however, note that ray map (100) still assumes a much higher growth rate for β: the global ray chaos already emerges for τ of order 20–30 km, whereas β approaches unity only for $\tau \simeq 500$ km. Such a strong reduction in the growth rate of β can be attributed to the fact that the wave corrections to the geometrical optics approximation commonly weaken the manifestation of ray chaos in the wave picture, similarly to what we have already seen in Section 5.2.3.

It seems reasonable to expect a sharper transition from the Poisson to Wigner statistics at a higher frequency of 600 Hz because of a weakening of the wave properties. A surprise, however, awaits us here. The sharp growth of parameter β with τ ceases at $\tau \simeq 120$ km and is replaced by a slow decrease of β stemming from the appearance of an increasingly larger number of degenerate eigenstates of the operator $\hat{G}$. The nature of this phenomenon becomes clear if we take into account that the origin of ray chaos in the presence of fast vertical oscillations of the perturbation is accompanied by bifurcations of periodic orbits (see Fig. 9). As shown in Refs [126, 127], strong fluctuations of spectral density occur in the vicinity of bifurcation points. Moreover, the amplitude of these fluctuations increases with the signal frequency, i.e., as the ray limit is approached.

Thus, the statistics of the spectrum of operator $\hat{G}$ contradict the ideas of random matrix theory in the presence of strong vertical oscillations of perturbation. This effect proves to be insignificant at a frequency of 200 Hz and does not noticeably affect the dependence of the Brody parameter β on τ, because the influence of bifurcations weakens with an increase in the wavelength.

6. Waveguides with random sound speed perturbations

6.1 Statistical description of ray chaos

The feasibility of a statistical description of the ray field structure stems from the fundamental property of the chaotic behavior of trajectories, which is called mixing [26, 27].

Let us consider a set of trajectories leaving a small domain $\mathcal{R}$ of a phase plane. For the distance $r \gg v^{-1}$, the points depicting these trajectories will be scattered over a much larger domain $\mathcal{R}'$. Mixing, in particular, implies that the fraction of trajectories that visit some subdomain of $\mathcal{R}'$, to be denoted as $\Delta\mathcal{R}'$, depends only weakly on the shape and size of the domain $\mathcal{R}$. The relative number of trajectories coming to $\Delta\mathcal{R}'$ (of those that left $\mathcal{R}$) can be interpreted as the probability of a trajectory getting into this subdomain. This definition of probability becomes more rigorous as $r \to \infty$ if simultaneously the size of $\mathcal{R}$ tends to zero. In our tasks, however, the finiteness of r is essential. We therefore cannot consider excessively small domains of initial conditions $\mathcal{R}$ or speculate about the probability of a ray visiting very small domains $\Delta\mathcal{R}'$.

To compute the statistical characteristics of the trajectory with the initial conditions $p(0) = p_0$ and $z(0) = z_0$, we consider a set of trajectories leaving a small domain $\mathcal{R}$ containing the point (p_0, z_0) as the statistical ensemble. We define the probability density for a ray to pass through the point (p, z) at the distance r through the relationship

$$P_{pz|p_0 z_0}(p, z, r|p_0, z_0) = \frac{1}{S_{\mathcal{R}}} \times \iint_{\mathcal{R}} \mathrm{d}p_0'\, \mathrm{d}z_0'\, \delta\big(z - z(r, p_0', z_0', r_0)\big)\, \delta\big(p - p(r, p_0', z_0', r_0)\big)\,, \qquad (116)$$

where $S_{\mathcal{R}}$ is the area of $\mathcal{R}$. The probability of a ray visiting the domain $\Delta\mathcal{R}'$ is given by the integral

$$P_{\Delta\mathcal{R}'} = \int_{\Delta\mathcal{R}'} \mathrm{d}p\, \mathrm{d}z\, P_{pz|p_0 z_0}(p, z, r|p_0, z_0)\,. \qquad (117)$$

As already mentioned, because of the finiteness of r, this definition gains some practical sense only for sufficiently large $\Delta\mathcal{R}'$, and, additionally, the domain of initial conditions $\mathcal{R}$ cannot be too small. For this reason, the probability density thus introduced can be applied to compute mean values of sufficiently smooth functions of p and z.

In a similar way, we define the probability density $P_{I\theta|I_0\theta_0}(I, \theta, r|I_0, \theta_0)$ in the action–angle coordinates: $P_{I\theta|I_0\theta_0}(I, \theta, r|I_0, \theta_0)$ gives the probability of the ray leaving the point (I_0, θ_0) to get into the vicinity of the observation point (I, θ). Treating the canonical transformation (22) as a nonlinear substitution of variables, connecting two pairs of random quantities, and taking into account that its Jacobian equals unity by virtue of the Liouville theorem (25), we find the link between the two probability densities introduced above:

$$P_{I\theta|I_0\theta_0}(I, \theta, r|I_0, \theta_0) = P_{pz|p_0 z_0}\big(p(I, \theta), z(I, \theta), r|p(I_0, \theta_0), z(I_0, \theta_0)\big)\,. \qquad (118)$$

Usage of the action–angle variables often enables substantial simplification of a statistical description of chaos: the angular variable θ makes a practice of rapidly 'forgetting' its initial value and can be considered as uniformly distributed in the interval $(0, 2\pi)$ already over quite short distances. In this case, one obtains

$$P_{I\theta|I_0\theta_0}(I, \theta, r|I_0, \theta_0) = \frac{1}{2\pi} P_{I|I_0}(I, r|I_0) . \tag{119}$$

The function $P_{I|I_0}(I, r|I_0)$ describes slow diffusion of rays over the action variable. A similar approach is widely applied for the analysis of chaotic dynamics in systems with periodic perturbation [26, 27].

If the perturbation is a realization of a random medium which is statistically homogeneous along the r-axis, the probability density defined by relationship (116) can only weakly depend on the particular realization of the random waveguide [37, 128–130]. This proposition, confirmed by numerical simulation results, hinges on the fact that initially close trajectories rapidly diverge under conditions of chaos over distances that exceed inhomogeneity correlation radii. On long paths, the rays intersect practically independent inhomogeneities and behave as if they were propagating in different realizations of a random medium. It is, therefore, natural to expect that averaging over initial conditions can lead to results resembling those obtained by averaging over the statistical ensemble of realizations.

6.2 Distributions of chaotic ray parameters

6.2.1 A model of randomly inhomogeneous USC. We present further the results of numerical modeling carried out for the waveguide model with the unperturbed sound speed profile $\bar{c}(z)$ (taken from Ref. [131]) depicted in Fig. 13a. This profile obeys formula (14) with the parameters $c_0 = 1.48$ km s^{-1}, $\varepsilon = 0.00238$, $z_{\text{th}} = 0.485$ km, and $z_{\text{a}} = 0.7$ km.

It is assumed that a weak perturbation $\delta c(r, z)$ originates from random internal waves with statistics defined by the widely known empirical Garrett–Munk spectrum [1]. Fluctuations of the sound speed $\delta c(r, z)$ are statistically homogeneous and isotropic in the horizontal plane. Their characteristic scales in this plane vary from several kilometers to several dozen kilometers. The intensity of fluctuations decays with the depth, and their characteristic vertical scales measure from several dozen to several hundred meters. To generate individual realizations of random field $\delta c(r, z)$, we used the method proposed in paper [50]. The realizations $\delta c(r, z)$ have been generated by adopting formula (19) of Ref. [50]. The spectrum of the perturbation dependence on the horizontal coordinate r is concentrated in the wave number interval from $2\pi/100$ km^{-1} to $2\pi/4$ km^{-1}, and the root-mean-square amplitude of δc is 0.5 m s^{-1} near the surface and drops with depth, according to the law $\exp(-z/L)$, where $L = 0.66$ km. Figure 13b plots the vertical sections of the field $\delta c(r, z)$ at three different distances.

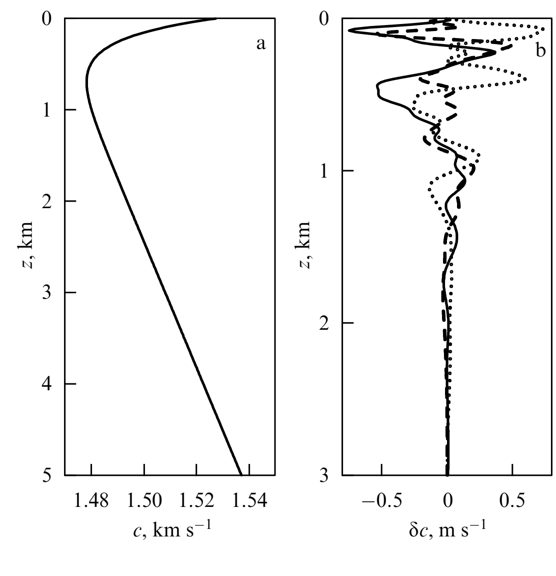

Figure 13. Unperturbed sound speed profile (a), and the vertical sections of perturbation δc at three different distances (b).

6.2.2 The Wiener process approximation. The method of approximately computing the function $P_{I|I_0}(I, r|I_0)$, presented in Refs [35–37, 43], exploits the fact that, since the perturbation is weak, the variable I changes only slightly on the typical longitudinal scale r_l of medium inhomogeneities (from several kilometers to several dozen kilometers). Because of this, the right-hand side of the Hamilton equation for action (26) can formally be treated as a delta-correlated random function. In this case, the dependence of ray action variable I on r is modelled by a Markovian random process, the probability density of which obeys the Fokker–Planck equation

$$\frac{\partial P_{I|I_0}}{\partial r} = \frac{1}{2} \frac{\partial}{\partial I} B(I) \frac{\partial P_{I|I_0}}{\partial I} . \tag{120}$$

The diffusion coefficient $B(I)$ can easily be assessed by resorting to numerical simulations of ray trajectories for concrete random medium realizations, performed with the help of a standard ray program [35–37, 43]. In our waveguide model, the quantity B weakly depends on I and can be replaced with the constant $B = 1.4 \times 10^{-7}$ km. The diffusion coefficients in other models of a deep-sea USC [37, 61, 128, 129, 132] have the same order of magnitude.

For a constant B, the dependence of the ray action on the distance can be represented in the form $I(r) = I_0 + x(r)$, where $I_0 = I(0)$, and $x(r)$ stands for the so-called Wiener random process [133, 134] satisfying the stochastic Langevin equation

$$\frac{dx}{dr} = \xi(r) , \tag{121}$$

where $\xi(r)$ is the white noise with a zero mean and correlation function $\langle \xi(r)\, \xi(r') \rangle = B\delta(r - r')$.

We call attention to the following important issue. The random function $x(r)$ defined by equation (121) can take both positive and negative values. However, the action variable I is nonnegative by definition. This circumstance is readily accounted for by introducing a reflecting boundary for trajectories $x(r)$ at $x = -I_0$ [37, 43, 129]. The possibility of introducing the boundary is an additional assumption. Its validity is confirmed by numerical modeling results.

If the boundary is present, the solution to the Fokker–Planck equation (120) with the initial condition $P_{I|I_0}(I, r|I_0) = \delta(I - I_0)$, which describes diffusive spreading (over I) of a bundle of rays with the same initial action I_0, takes the form

$$P_{I|I_0}(I, r|I_0) = \frac{1}{\sqrt{2\pi Br}} \times \left[\exp\left(-\frac{(I - I_0)^2}{2Br} \right) + \exp\left(-\frac{(I + I_0)^2}{2Br} \right) \right] . \tag{122}$$

If the condition

$$Br \ll I_0 \tag{123}$$

holds true, the ray action variable on the path to the observation point r does not manage to approach the value of $I = 0$, and the reflecting boundary is not needed. This condition holds for rays with sufficiently large initial grazing angles χ_0 (I_0 increases monotonically with the growth in $|\chi_0|$). We will therefore call the rays obeying condition (123) steep. The second term on the right-hand side of formula (122) can be neglected when describing them. The variance of the action variable for a steep ray grows with distance according to the diffusion law

$$\sigma_I \equiv \left\langle (I - I_0)^2 \right\rangle^{1/2} = Br\,. \tag{124}$$

Numerical simulations indicate that, for estimates, condition (123) can partly be relaxed, with the requirement that $\ll$ be replaced by $<$. In our waveguide model, such a condition is valid for rays grazing at angles $\chi > 5°$ on the waveguide axis at a distance of $r = 3000$ km.

Hamilton equation (27) for the variable θ can also be approximately replaced by a very simple Langevin stochastic equation. Let us neglect the second term on the right-hand side of Eqn (27) and replace $\omega(I)$ by the function $\omega(I_0) + \omega'(I_0)x$ [35–37]. Representing the angular variable as $\theta(r) = \theta_0 + \omega(I_0)r + y(r)$, where $\theta_0 = \theta(0)$, and $\theta_0 + \omega(I_0)r$ is the ray angular variable at the distance r in the unperturbed waveguide, we obtain the stochastic equation

$$\frac{\mathrm{d}y}{\mathrm{d}r} = \omega'(I_0)x\,. \tag{125}$$

Hence, it follows that, for steep rays, the variance of the angular variable reduces to

$$\sigma_\theta \equiv \left\langle (\theta - \theta_0)^2 \right\rangle^{1/2} = \left|\omega'(I_0)\right| \left(\frac{B}{3}\right)^{1/2} r^{3/2}\,. \tag{126}$$

At short distances, where the ray action variables differ only slightly from their initial values, the ray trajectory distortion is largely determined by perturbations of the angular variable, i.e., the function $y(r)$. According to equation (125), its magnitude is proportional to $\omega'(I_0)$. This implies that the sensitivity of the ray trajectory to the influence of sound speed fluctuations depends to a substantial extent on the derivative of $\omega'(I_0)$, which in turn is set solely by the unperturbed sound speed profile $\bar{c}(z)$. This agrees perfectly well with the results of papers [61, 73, 74, 87, 135], in which it is proved that the sensitivity of ray trajectories to the perturbation $\delta c(r, z)$ is defined by the stability parameter α given by relationship (50). The numerical modeling results presented in these papers confirm that the instability of trajectories indeed increases with α.

We call the replacement of Hamilton equations (26) and (27) by the stochastic equations (121) and (125) the *Wiener process approximation*. Numerical simulations indicate that this approximation describes fairly well the statistical properties of rays on paths measuring thousands of kilometers. Let us demonstrate it with a particular example. We are going to explore the applicability of relationships (119) and (122).

Formulas (119) and (122) describe the distribution of action variables of rays with initial conditions in a small domain $\mathcal{R}$ of a phase plane. Figure 14 presents the results of numerical trajectory computations for the rays emanating from domains $\mathcal{R}$ shown in Fig. 14a, c, e with small black rectangles. Figure 14a, b exhibits the rays coming from depths z close to the waveguide z_a-axis, at initial grazing angles of about 3°. The trajectories of 10,000 rays with initial parameters (p_0, z_0) uniformly filling the black rectangle in Fig. 14a were computed to the distance $r = 3000$ km with the help of a ray program. The randomly scattered points in Fig. 14a display the distribution of these rays in the phase plane (p, z) for a particular realization of random perturbation $\delta c(r, z)$. The action distribution for these rays is presented by one of stepwise lines in Fig. 14b, which displays a normalized histogram. The second stepwise line is the histogram of analogous distribution computed for another realization of perturbation $\delta c(r, z)$. The normalized histograms are compared with the probability density for the action variable I, predicted by formula (122) (smooth curve). Analogous results for rays emanating at angles close to 6° and 9° are plotted in Fig. 14c, d and e, f, respectively. This and other comparisons of the theory to numerical simulations confirm not only the applicability of formula (122), but also our assumption that the ray statistics on long paths are only weakly dependent on the concrete realization of random medium inhomogeneities.

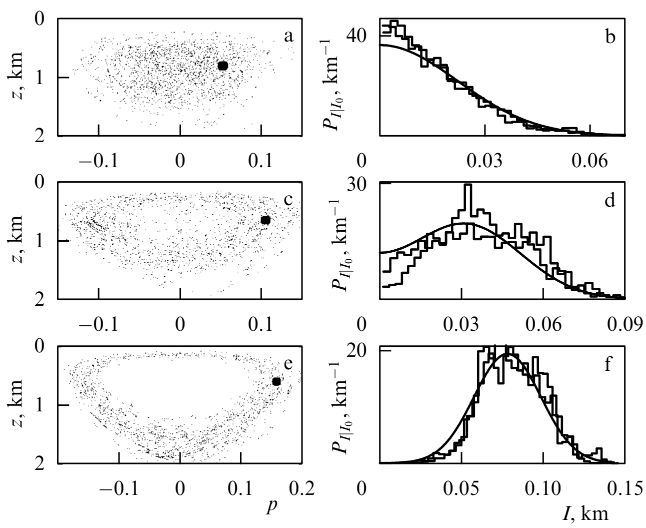

Figure 14. The distribution of rays leaving a small domain $\mathcal{R}$ of a phase plane. Three selected domains $\mathcal{R}$ in panels a, c, and e are indicated by small black rectangles. Points scattered in a random way show the coordinates of rays (leaving the respective rectangles) at a distance of 3000 km. Panels b, d, and f display the distributions of ray action variables I at this distance. The stepwise lines are the normalized diagrams obtained through numerical simulations of ray trajectories for two realizations of perturbation $\delta c(r, z)$. The smooth curves fit the probability densities predicted by formula (122). The initial ray depths for all rectangles are close to the axis of the USC. The initial grazing angles are close to 3° (panels a and b), 6° (panels c and d), and 9° (panels e and f).

6.2.3 A point source field. For a point source, the initial coordinates of the rays lie on the straight line $z = z_s$ in the phase plane $p-z$, where z_s is the source depth. We demonstrate how formula (122) can be applied to describe the statistics of these rays.

Assume the initial momenta to be confined to the interval $-p_{\max} < p_0 < p_{\max}$. The probability density of p_0 will formally be considered $(2p_{\max})^{-1}$ in this interval, and zero outside it. Such a choice of the probability density is in fact concerned with the assumption that the directivity pattern of

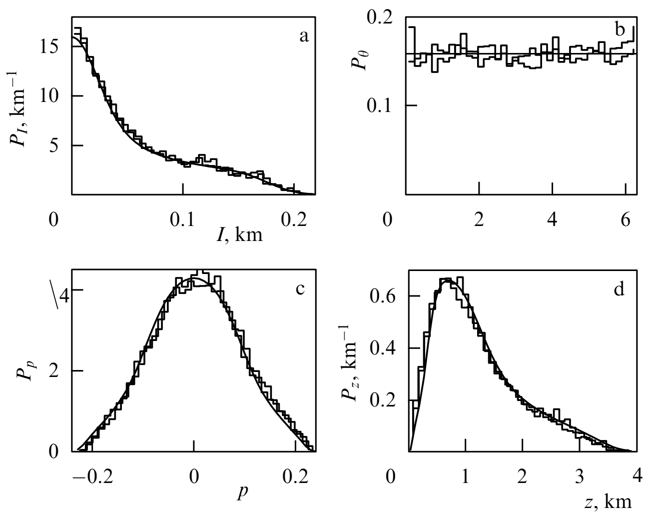

Figure 15. The distributions of ray parameters at a distance of $r = 3000$ km. The smooth curves plot the probability densities of I (a), θ (b), p (c), and z (d) found in the Wiener process approximation for rays emanating from a point source at the depth $z_s = 0.7$ km. The stepwise lines represent normalized histograms constructed on the base of numerical simulations of ray trajectories for two realizations of perturbation $\delta c(r, z)$.

the source at hand is isotropic within the angular interval set by the choice of $p_{\max}$.

At distances of about 1000 km, where formula (119) is applicable, the probability density for the action variable is defined as

$$P_I(I, r) = \frac{1}{2p_{\max}} \int_{-p_{\max}}^{p_{\max}} \mathrm{d}p_0 \, P_{I|I_0}\big(I, r | I(p_0, z_0)\big) \, . \tag{127}$$

The function $I(p_0, z_0)$ in the integrand is given by canonical transform (22). With account for relationship (118), the joint probability density of the momentum and coordinate at the distance r is expressed as

$$P_{pz}(p, z, r) = \frac{1}{2\pi} \, P_I\big(I(p, z), r\big) \, . \tag{128}$$

Integrating last formula over p and z, we find the probability densities for z and p, respectively. In particular, for z we obtain

$$P_z(z, r) = \frac{1}{4\pi p_{\max}} \times \int \mathrm{d}p \int_{-p_{\max}}^{p_{\max}} \mathrm{d}p_0 \, P_{I|I_0}\big(I(p, z), r | I(p_0, z_0)\big) \, . \tag{129}$$

The smooth curves in Fig. 15 display the probability densities for I, θ, and p on a path of 3000 km, computed in the Wiener process approximation, i.e., based on formulas (122), (127), and (129) (for the angular variable θ modulo 2π, we expect a uniform distribution). It is assumed that $\eta(p_0) = 1/(2p_{\max})$, i.e., the source directivity pattern is approximately isotropic. These curves are compared with probability density estimates (normalized histograms) obtained from numerical simulations of 48,000 rays. The computations were performed for a point source at 0.7 km depth, and the initial angles of emergent rays fall in the range $\pm 12°$. As is apparent, predictions made in the Wiener process approximation agree well with the numerical modeling results.

6.3 Smoothed wave field intensity

In this section, we will show how the knowledge of ray statistical characteristics can be exploited to assess the sound field intensity. We will be dealing with the estimate of spatial intensity distribution which is smoothed along the vertical coordinate.

On ray paths measuring thousands of kilometers, the field at an observation point is formed by a huge number of chaotic rays. A smoothed distribution of field intensity, defined by the relationship

$$J(r, z) = \frac{1}{\sqrt{2\pi}\varDelta_z} \int \mathrm{d}z' \, \big|u(r, z')\big|^2 \exp\left[-\frac{(z - z')^2}{2\varDelta_z^2}\right] , \tag{130}$$

where $\varDelta_z$ is the smoothing scale, can be estimated through the noncoherent summation of their contributions [3]. According to expression (18), the sum of intensities of eigenrays at the observation point can be written out as

$$\begin{aligned} \big|u(r, z)\big|^2 &= \sum_j \frac{k}{2\pi|\partial z/\partial p_0|}\bigg|_{p_0 = p_{0,j}} \\ &= \frac{k}{2\pi} \int_{-p_{\max}}^{p_{\max}} \mathrm{d}p_0 \, \delta\big(z - z(r, p_0, z_s)\big) \, , \end{aligned} \tag{131}$$

where the index j numbers the rays arriving at the point (r, z). We divide the interval $(-p_{\max}, p_{\max})$ of initial momentum values into many small subintervals with boundary points p_n, $n = 1, \ldots, N$. Let us represent the last expression in Eqn (131) in the form

$$\big|u(r, z)\big|^2 = \frac{k}{2\pi} \sum_{n=1}^{N-1} \int_{p_{n-1}}^{p_n} \mathrm{d}p_0 \, \delta\big(z - z(r, p_0, z_s)\big) \, , \tag{132}$$

where each of integrals has a form that coincides with that of the right-hand side of relationship (116) in the case where the domain $\mathcal{R}$ degenerates into a section of the p-axis. According to Eqns (116) and (118), one finds

$$\begin{aligned} \int_{p_n}^{p_{n+1}} \mathrm{d}p_0 \, \delta\big(z - z(r, p_0, z_s)\big) &= (p_{n+1} - p_n) \\ &\times \int \mathrm{d}p \, P_{pz|p_0 z_0}(p, z | p_j, z_s) \\ &= \frac{p_{n+1} - p_n}{2\pi} \int \mathrm{d}p \, P_{I|I_0}\big(I(p, z), r | I(p_j, z_s)\big) \, , \end{aligned} \tag{133}$$

where the integration is carried out over all possible values of p. Substituting Eqn (133) into Eqn (132) and substituting $p_{n+1} - p_n \to \mathrm{d}p_0$, we obtain

$$\big|u(r, z)\big|^2 = \frac{k}{(2\pi)^2} \int_{-p_{\max}}^{p_{\max}} \mathrm{d}p_0 \int \mathrm{d}p \, P_{I|I_0}\big(I(p, z), r | I(p_j, z_s)\big) . \tag{134}$$

This relationship can be rewritten as

$$\big|u(r, z)\big|^2 = \frac{p_{\max} k}{\pi} \, P_z(z, r) \, , \tag{135}$$

where $P_z(z, r)$ is the probability density of coordinate (129). The substitution of Eqn (135) into Eqn (130) yields [133]

$$J(r, z) = \frac{2kp_{\max}}{(2\pi)^{3/2}\varDelta_z} \int \mathrm{d}z' \, \exp\left(-\frac{(z - z')^2}{2\varDelta_z^2}\right) P_z(z', r) . \tag{136}$$

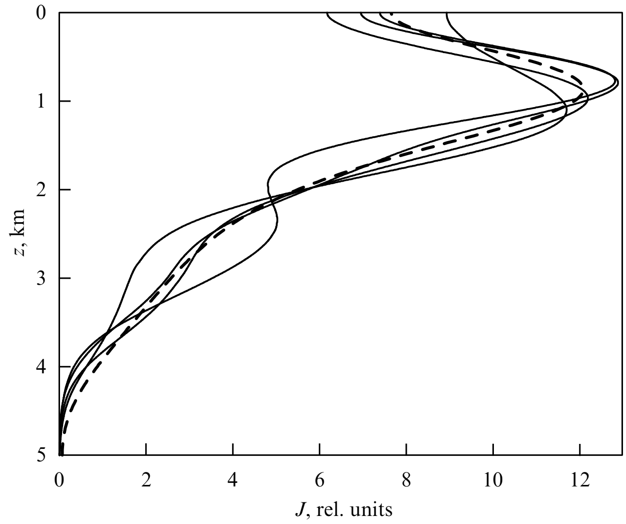

Figure 16. The dependence of smoothed field intensity J at a distance of 3000 km on the depth z. The carrier frequency $f = 75$ Hz. The dashed line is the prediction of formula (136). The solid lines correspond to numerical solutions of the parabolic equation for four realizations of random perturbation.

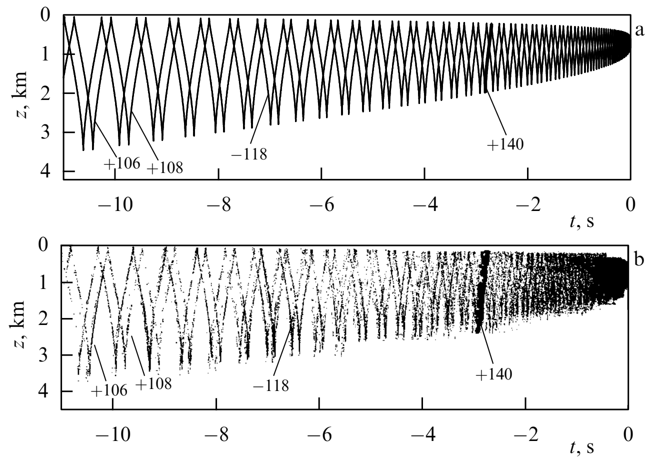

Figure 17. Timefronts ($t-z$ diagrams) in the unperturbed (a) and perturbed (b) waveguides: the distributions of ray travel times in the time–depth plane at a distance of 3000 km from a point source at the depth $z_s = 0.7$ km. Some of segments are labelled with values of identifiers that correspond to them. In panel a, the arrivals of rays with identifier +140 are plotted with the thick solid line, but in panel b the arrivals of rays with the same identifier (fuzzy segment) are plotted with thick dots.

Figure 16 compares the prediction made with formula (136) (dashed curve) to the results obtained through computations of smoothed intensity by numerically solving the parabolic equation at a carrying frequency of 75 Hz for four realizations of random perturbation. The smoothing scale Δ_z of 0.4 km was selected. Apparently, formula (136) offers a rough but correct estimate by the order of magnitude for the smoothed intensity.

6.4 Travel times of chaotic rays

6.4.1 The effect of travel time clustering. As discussed in Section 4, extensive experimental material has been accumulated to date on sound propagation along distances of about 1000 km (see, for example, Refs [1, 136]). A remarkable property of fields in deep-sea acoustic waveguides, which was already known in the 1970s, is the unexpectedly high stability of the initial part of the received signal, formed by steep rays. Sound pulses propagating along rays grazing at rather large angles yield to detection and identification with relative ease, and their arrival times can be computed with good accuracy in the framework of the simplest medium model, without account for fluctuations δc caused by internal waves [55]. It is for this reason that the ray travel times are considered to be the main input parameters for the solution to inverse problems in systems of acoustic monitoring of the ocean temperature field [55, 137, 138].

At first glance, it seems surprising that a part of the signal remains stable even in the presence of inhomogeneities δc conductive to the ray chaos. The unperturbed model of the waveguide enables the correct prediction of the peak positions in the initial parts of signals recorded over distances 3–5 thousand kilometers in length, where the ray chaos is already well developed [16, 28, 63]. An explanation of this effect (although not exhaustive) was proposed in the second half of the 1990s, when it had become clear that arrival times of chaotic rays to an observation point tend to form stable *clusters* [13, 15, 19]. The ray characteristic called the *identifier* and denoted as $\pm M$ acquires the principal role in their description. The definition of the identifier was given in Section 2.3.

Numerical simulations show that each cluster is formed by rays with the same identifier, i.e., with the same topology. The cluster center is close to the arrival time of the unperturbed (regular) ray with the identifier equal to that of chaotic rays forming the cluster. Those stable peaks that are resolved in both field and numerical experiments, and are associated with the arrivals of steep unperturbed rays, are in fact formed by groups of ray pulses reaching the receiving point along chaotic trajectories with the same topology. On long paths, rays with the same identifiers may substantially diverge from each other in space at intermediate distances [19].

To illustrate these statements, consider $t-z$ diagrams, i.e., the distributions of ray arrivals in the time–depth plane (see Section 2.3), at a distance of 3000 km in unperturbed ($\delta c = 0$) and perturbed waveguides, plotted in Fig. 17a and b, respectively. To construct them, trajectories of 50,000 rays emanated by a point source at the depth $z_s = 0.7$ km with initial grazing angles in the interval $\pm 12°$ have been computed by numerically integrating Hamilton equations in the unperturbed and perturbed waveguides. Each point of the diagram corresponds to the arrival of a single ray. In Figure 17a (unperturbed waveguide), the points form continuous piecewise broken lines. The dependence between the ray travel time and its vertical coordinate is also given by a continuous function in the perturbed waveguide (Fig. 17b). However, this dependence under the conditions of chaos becomes so complex on long paths that our bundle of rays turns out to be insufficiently dense to visualize its continuity. The random scatter of points in the $t-z$ diagram indicates the ray chaos. When recording signals at the depth z_0, the ray travel times are determined by the intersections of the $t-z$ diagram with the horizontal straight line $z = z_0$. In the unperturbed waveguide, the intersection with each diagram segment (a portion of the broken line) specifies a single ray.

Each segment of the $t-z$ diagram in the unperturbed waveguide is formed by rays with *equal* identifiers. In the

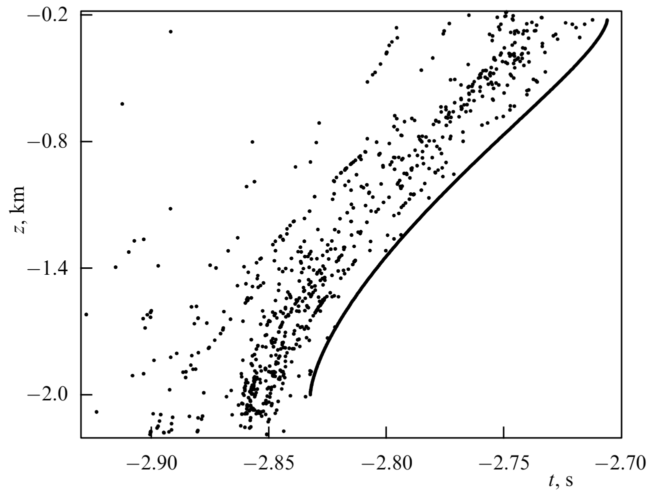

Figure 18. The arrivals of rays with identifier +140 at a distance of 3000 km in the time–depth plane in the perturbed (points) and unperturbed (solid curve) waveguides.

analogous diagram for the perturbed waveguide, the arrivals of rays with a given identifier form compact groups of points, which we call *fuzzy* segments. The section of fuzzy segment of the straight line $z = z_r$ determines the cluster of ray travel times for a point receiver at the depth z_r. Figure 17 indicates that segments formed by steep rays do not substantially differ on the initial parts of $t-z$ diagrams in the unperturbed and perturbed waveguides. This fact precisely reflects the stability of the initial part of the received signal, alluded to above.

Figure 17 also displays ray identifiers for selected parts of the diagrams.

Looking at Fig. 18, which shows rays with the identifier +140, marked in Fig. 17, we conclude that the perturbation δc leads not only to spreading the $t-z$ diagram segments but also to their left *displacement* toward shorter times.

The similarity of the initial parts of $t-z$ diagrams notwithstanding, the dependence of ray travel times on the angles at which the rays leave the source is cardinally different in the unperturbed and perturbed waveguides. If we select a certain unperturbed ray and start monotonically varying its emerging angle χ_s, the respective point in the $t-z$ diagram will monotonically move along the piecewise broken line passing from segment to segment. Acting in the same manner in the perturbed waveguide, we will see that the point mapping the ray in the $t-z$ diagram 'jumps' chaotically in the time–depth plane. This chaos, however, preserves nontrivial regularity: in the initial part of the $t-z$ diagram, the point moving chaotically always stays in the vicinity of segments of the unperturbed diagram, 'running' from one unperturbed segment to another (not necessarily neighboring) and returning back.

6.4.2 Estimates of scatter in chaotic ray travel times. The description of a cluster hinges on an approximate formula for the difference in travel times between perturbed and unperturbed rays joining the point source and receiver and possessing the same identifiers [35, 37, 74, 139, 140]. This formula has the form

$$\delta t = \delta t_V + \delta t_I \,, \tag{137}$$

where

$$\delta t_V = -\frac{1}{c_r^2} \int \mathrm{d}r \, \delta c\big(r, z(r)\big) \,, \tag{138}$$

$$\delta t_I = \frac{\omega'(\bar{I})}{2c_r} \int_0^r \mathrm{d}r' \, \big(I(r') - \bar{I}\big)^2 \,, \tag{139}$$

$\bar{I}$ is the action variable of an unperturbed ray, and $I(r)$ is the dependence of the perturbed ray action on the distance. On relatively short paths (several hundred kilometers), a weak perturbation does not manage to substantially distort ray trajectories, and the coincidence of identifiers for the perturbed and unperturbed rays in fact implies the coincidence of their trajectories. In this case, the main contribution to δt comes from sound speed fluctuations δc along the unperturbed trajectory $z(r)$. The term δt_I on the right-hand side of Eqn (137) can be omitted on short paths, and we arrive at the well-known result: $\delta t = \delta t_V$ [1, 55]. The width of the cluster, estimated as $\langle (\delta t_V)^2 \rangle^{1/2}$, grows with distance proportionally to $r^{1/2}$. At distances measuring several hundred kilometers, the typical magnitude of δt_V is several milliseconds.

Another mechanism dominates on paths of the order of several thousand kilometers. It relates to strong changes in the form of ray trajectory occurring under the influence of the perturbation δc. In this case, the right-hand side of formula (137) is governed by the term δt_I. To analyze its statistical characteristics, one may apply the approach discussed in Sections 6.1 and 6.2 and show that the mean cluster displacement is defined by the formula [35, 37, 139, 140]

$$\langle \delta t_I \rangle = \frac{\omega'(\bar{I})}{12 c_r} \, B r^2 \,, \tag{140}$$

while its spread $\big\langle (\delta t_I - \langle \delta t_I \rangle)^2 \big\rangle^{1/2}$ is approximately $|\langle \delta t_I \rangle|$. According to Eqns (139) and (140), the direction of cluster displacement is determined by the sign of the derivative of $\omega'(I)$. In typical deep-sea waveguides, the length of the ray cycle increases with the grazing angle on the waveguide axis. This implies that $\omega'(I)$ is typically negative, and that the cluster displaces toward shorter times, as we have seen in Fig. 18. According to the available estimates, the cluster width on long paths grows with distance proportionally to r^2 and amounts to approximately 0.01 s or 0.1 s for, respectively, steep or flat rays at a distance of 3000 km.

Admittedly, the link between the ray travel times and amplitudes remains as yet unstudied. This question, however, is very important because the rays forming the cluster generally have essentially different amplitudes and, consequently, contribute differently to the signal peak associated with a given cluster.

Reference [19] considers a numerical example showing that, despite a huge number of rays forming a cluster, the peak that corresponds to this cluster is in fact formed by pulses with maximum amplitudes arriving along just several rays. The scatter in travel times for these rays is relatively small, and the peak can be 5–10 times tighter than the full cluster.

When discussing clusters, we were comparing the travel times of rays reaching one and the same point in space and having the same identifiers. We now turn to the estimate of travel time scatter for a bundle formed by rays radiated at angles in the vicinity of some fixed angle χ_0. In this case, the initial values of variable I are nearly the same for all rays: $I_0 \equiv I(\chi_0)$. At distances of about 1000 km, where the chaos is already well developed, the rays of this bundle not only explore different depths but, generally speaking, also have different identifiers. An approximate formula expressing the arrival time difference for rays with identifiers $\pm(M + \Delta M)$ and $\pm M$ has the form [35, 37, 139, 140]

$$\delta t = \frac{4\pi \Delta M I_0}{c_r} \,. \tag{141}$$

For $\Delta M \neq 0$, this quantity commonly by far exceeds (in absolute value) δt_V and δt_I. Estimating ΔM as $\langle(\theta - \theta_0)^2\rangle^{1/2}/\pi$ and making use of formula (126), we find

$$\langle \delta t^2 \rangle^{1/2} = \left|\omega'(I_0)\right| \frac{r^{3/2}}{c_r} \left(\frac{B}{3}\right)^{1/2} . \tag{142}$$

Hence, it follows that the scatter in ray travel times grows proportionally to $r^{3/2}$. Such a distance dependence agrees well with the results of other authors [74]. At a distance of 3000 km, estimate (142) gives a value of order 1 s, which exceeds the cluster width by one or two orders of magnitude. This result once again indicates how strongly the ray travel time depends on the trajectory topology.

6.5 Smoothed distribution of sound energy over waveguide normal modes

In Section 2.6 we presented simple analytical relationships which enabled the amplitudes of normal modes to be expressed in terms of ray trajectory parameters. With their assistance, the stochastic ray theory based on the Wiener process approximation can be applied to the analysis of field mode structure. We demonstrate this here by computing, as an example, the intermodal redistribution of sound energy that accompanies scattering on sound speed fluctuations $\delta c(r, z)$. The quantities $|a_m(r)|^2$ will, for the sake of brevity, be termed the intensities of normal modes. Our goal is an estimate of smoothed modal intensities

$$J_m(r) = \sum_{m'} \left|a_{m'}(r)\right|^2 \exp\left[-\frac{(m - m')^2}{2\mu^2}\right] \times \left\{\sum_{m'} \exp\left[-\frac{(m - m')^2}{2\mu^2}\right]\right\}^{-1} , \tag{143}$$

where μ is the smoothing scale. As in Section 6.3, which dealt with the analogous task of computing smoothed sound field intensity (130), we make use of noncoherent ray summation. However, while Section 6.3 operated with the summation of eigenrays forming the field at a given waveguide point, here we have to sum the contributions from modal rays that form the mode field. Under ray chaos conditions, the number of modal rays becomes very large, they are practically independent, and it is natural to expect that a rough estimate of J_m can be obtained by summing their intensities. The results of numerical modeling performed in Refs [49, 141] lend support to this conjecture.

Consider a situation where the initial field obeys formula (33), i.e., only a single mode with the order m_0 is excited at $r = 0$. In this case, the analog of formula (131) for the mode intensity, according to Eqns (35) and (36), becomes

$$\left|a_m(r)\right|^2 = \frac{1}{2\pi k} \sum_j \frac{1}{\left|\partial I(r, I_{m_0}, \theta_0)/\partial\theta_0\right|_{\theta_0 = \theta_{0,j}}} = \frac{1}{2\pi k} \int_0^{2\pi} \mathrm{d}\theta_0 \, \delta\big(I_m - I(r, I_{m_0}, \theta_0)\big) \,, \tag{144}$$

where the index j enumerates the modal rays. The integral in the last expression can be transformed just as the integral on the right-hand side of formula (131). Dividing the interval of integration over θ_0 into small subintervals, we note that integrals over each of them are also analogous to the integral in relationship (116). For the subinterval $(\theta_0, \theta_0 + \delta\theta)$, we have

$$\frac{1}{\delta\theta} \int_{\theta_0}^{\theta_0 + \delta\theta} \mathrm{d}\theta_0 \, \delta\big(I_m - I(r, I_{m_0}, \theta_0)\big) = P_I(I_m, r | I_{m_0}) \,. \tag{145}$$

Since the right-hand side is independent of θ_0, we obtain

$$\left|a_m(r)\right|^2 = \frac{1}{k} \, P_I(r, I_m | I_{m_0}) \,. \tag{146}$$

Assuming $m \gg \mu$, the integration limits over m' can formally be moved to infinity. In that case, one-finds

$$\sum_{m'} \exp\left[-\frac{(m - m')^2}{2\mu^2}\right] \simeq \int_{-\infty}^{\infty} \mathrm{d}m' \, \exp\left[-\frac{(m - m')^2}{2\mu^2}\right] = \sqrt{2\pi}\,\mu \,. \tag{147}$$

We approximate the summation over m in formula (143) by integration, as in Eqn (147). Then, formally replacing m with $kI + 1/2$ [based on quantization rule (29)], we go over from the integration over m to integration over I:

$$J_m(r) = \frac{1}{\sqrt{2\pi}\,\mu} \int \mathrm{d}I' \, P_I(r, I' | I_{m_0}) \exp\left[-\frac{k^2 (I_m - I')^2}{2\mu^2}\right] . \tag{148}$$

We take advantage of relationship (122), which gives the explicit expression for function $P_I(r, I | I_0)$. For modes with high orders, which are formed by steep rays satisfying condition (123), the second term on the right-hand side of Eqn (122) can be neglected, and the integration limits over I' can formally be shifted to infinity. In this case, one obtains

$$J_m(r) = \frac{1}{\sqrt{2\pi(\mu^2 + k^2 Br)}} \exp\left[-\frac{(m - m_0)^2}{2(\mu^2 + k^2 Br)}\right] . \tag{149}$$

At a frequency of 75 Hz, formula (149) is only applicable to modes with orders $m > 7$. In order to describe the modes with smaller wave numbers, we have to account for both terms on the right-hand side of Eqn (122), as well as for the finiteness of a lower integration limit. Note that according to Eqn (149) the number of effectively excited modes increases with distance as $r^{1/2}$ on very long paths. This dependence was also found in Ref. [142] by analyzing numerical simulation results.

To test the applicability of estimate (149), we numerically solved parabolic equation (7) at a carrying frequency of 75 Hz with the initial condition $u(0, z) = \varphi_{24}(z)$. The intensities of modes at a distance of 3000 km are exhibited in Fig. 19a for two realizations of random perturbation. Figure 19b plots the results for the smoothed intensity with the smoothing scale $\mu = 4$. The solid lines show intensities J_m computed by directly, numerically solving the parabolic equation for four perturbation realizations (values $|a_m|^2$ for two of these realizations are given in Fig. 19a). The dashed line corresponds to the prediction of formula (149). Notably, the smoothed intensity shows no strong sensitivity to the perturbation realizations, and our analytical estimate satisfactorily agrees with numerical simulation results. Reference [37] reports that smoothed mode inten-

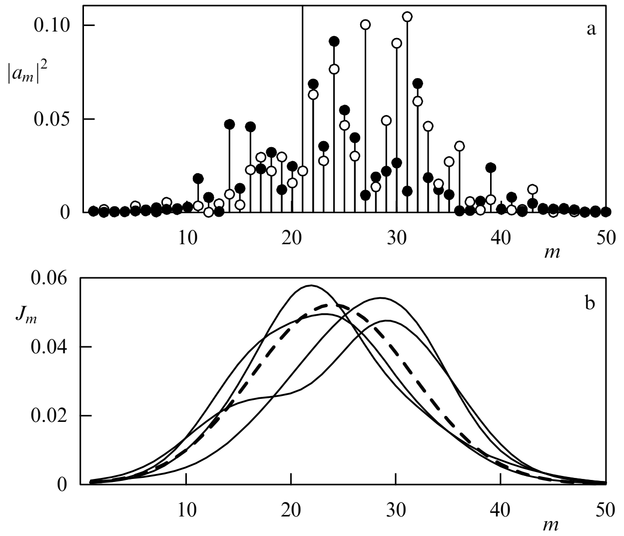

Figure 19. Mode intensities when at $r = 0$ a single mode with number 24 ($u(0, z) = \varphi_{24}(z)$) is excited at a carrying frequency of 75 Hz. (a) Mode intensities for two perturbation realizations (white and black circles). (b) Smoothed mode intensities computed for four perturbation realizations (solid curves) and the prediction of formula (149) (dashed line). The smoothing scale $\mu = 4$.

sities can be computed in just the same way as in the case of a point source.

Making use of the relationships expressing the mode amplitudes in terms of ray trajectory parameters enables the analysis of field mode structure not only for a monochromatic, but also for a pulse source. The investigation of sound pulses transferred by separate modes is beyond the scope of this review. This question is thoroughly discussed in Refs [43, 130].

7. Conclusions

In this review, by discussing concrete examples we tried to describe the main tasks arising in the research of ray and wave chaos in underwater acoustic waveguides. We considered two models of waveguides: with periodic inhomogeneities of the speed of sound, and with inhomogeneities given by realizations of a random field. At first glance, it may seem that the properties of ray and wave chaos in these models are cardinally different. In contrast to the phase space structure in a periodic waveguide, which breaks into subdomains with absolutely different properties (the chaotic sea and stability islands), the phase space structure in models with random inhomogeneities seems rather uniform. However, in essence, this is not the case. Because of significant scatter in the Lyapunov exponents [19], at any finite distance there are bundles of weakly diverging rays which form analogs of stability islands. Although the fraction of such rays at long distances is small, their contribution to the net wave field may play a decisive role [19].

Despite the seemingly artificial character of periodic models, it was exactly these that laid the basis to exploring chaos in underwater acoustics. For one thing, they benefited from the direct use of the powerful methods of dynamical and quantum chaos theory, such as the methods of the Poincaré map or quasistationary states (Floquet states) [23]. Studying such models helps us to understand the general properties of chaotic ray dynamics and can hint at new research avenues for the analysis of waveguides with other types of inhomogeneities. We argue that the 'potential' of periodic models is not yet exhausted, and results obtained with their assistance can have analogs in real underwater sound channels.

One of the goals of ray chaos studies consists in finding out limitations imposed by this phenomenon on the mere feasibility of solving inverse problems pertaining to the reconstruction of the large-scale structure of the oceanic temperature fields. From this viewpoint, it seems extremely important to search for sound field characteristics that remain stable in the face of refractive index fluctuations in the field of internal waves. An example of such characteristics is furnished by the travel time clusters discussed in Section 6.4. Owing to the clustering effect, even at distances as long as several thousand kilometers, one can distinguish the contributions from large-scale temperature field inhomogeneities in temporal variations of the received signal structure (under the conditions of developed ray chaos). Notice, incidentally, that an important contribution to understanding the clusterization effect came from the studies of travel times in a periodic waveguide model, performed in Ref. [15].

To conclude, we note that the research of wave chaos is to a substantial degree hindered by an insufficient understanding of the applicability bounds of the geometrical optics method. We know that some of its predictions remain valid at distances in the range of thousands of kilometers, in essence, at least from numerical simulations and from comparisons of theoretical results with the data of field observations. Similar difficulties arise in quantum chaos theory, as well. In our opinion, of promise are the studies exploring the utility of the ray approach for assessing the field characteristics smoothed over temporal, angular, and spatial scales. Numerical simulations indicate that by choosing sufficiently large smoothing scales one frequently succeeds in compensating for the errors of ray approximation. The scales of smoothing, however, require empirical tuning at the current stage.

Acknowledgments

The work was carried out under the partial financial support from the RFBR (projects Nos 09-05-98520, 09-05-98608, 10-02-00228, 11-01-12057), the RAS programs 'Fundamental Problems of Nonlinear Dynamics' and 'Fundamental Principles of Acoustical Diagnostics of Artificial and Natural Media', a grant from the President of the Russian Federation (MK-4324.2009.5), the grants 'Leading Scientific Schools' NSh-3700.2010.2 and FTsP 'Scientific and Scientific-Pedagogical Personnel of Innovative Russia' (contract No. 02.740.11.0565), and a grant from the Dynasty Foundation.

The authors are indebted to M Yu Uleysky, E V Kononchik, A Yu Kazarova, and L Ya Lyubavin for assistance in preparing the material.

References

1. Flatté S M et al. *Sound Transmission Through a Fluctuating Ocean* (Ed. S M Flatté) (Cambridge: Cambridge Univ. Press, 1979)
2. Brekhovskikh L M, Lysanov Yu P *Teoreticheskie Osnovy Akustiki Okeana* (Fundamentals of Ocean Acoustics) (Moscow: Nauka, 2007) [Translated into English (New York: Springer, 2003)]
3. Jensen F B et al. *Computational Ocean Acoustics* (New York: AIP Press, 1994)
4. Munk W H et al. *J. Acoust. Soc. Am.* **96** 2330 (1994)

5. Abdullaev S S, Zaslavskii G M *Zh. Eksp. Teor. Fiz.* **80** 524 (1981) [*Sov. Phys. JETP* **53** 265 (1981)]
6. Abdullaev S S, Zaslavskii G M *Zh. Eksp. Teor. Fiz.* **85** 1573 (1983) [*Sov. Phys. JETP* **58** 915 (1983)]
7. Abdullaev S S, Zaslavskii G M *Zh. Eksp. Teor. Fiz.* **87** 763 (1984) [*Sov. Phys. JETP* **60** 435 (1984)]
8. Abdullaev S S, Zaslavskii G M *Izv. Akad. Nauk SSSR. Ser. Fiz. Atmos. Okeana* **23** 724 (1987)
9. Abdullaev S S, Zaslavskii G M *Akust. Zh.* **34** 578 (1988) [*Sov. Phys. Acoust.* **34** 334 (1988)]
10. Abdullaev S S, Zaslavsky G M *Usp. Fiz. Nauk* **161** (8) 1 (1991) [*Sov. Phys. Usp.* **34** 645 (1991)]
11. Abdullaev S *Chaos and Dynamics of Rays in Waveguide Media* (Langhorne, Pa.: Gordon and Breach, 1993)
12. Palmer D R et al. *Geophys. Res. Lett.* **15** 569 (1988)
13. Palmer D R, Georges T M, Jones R M *Comput. Phys. Commun.* **65** 219 (1991)
14. Smith K B, Brown M G, Tappert F D *J. Acoust. Soc. Am.* **91** 1939 (1992)
15. Tappert F D, Tang X *J. Acoust. Soc. Am.* **99** 185 (1996)
16. Simmen J, Flatté S M, Wang G-Y *J. Acoust. Soc. Am.* **102** 239 (1997)
17. Wolfson M A, Tappert F D *J. Acoust. Soc. Am.* **107** 154 (2000)
18. Wolfson M A, Tomsovic S *J. Acoust. Soc. Am.* **109** 2693 (2001)
19. Beron-Vera F J et al. *J. Acoust. Soc. Am.* **114** 1226 (2003)
20. Worcester P F, Spindel R C *J. Acoust. Soc. Am.* **117** 1499 (2005)
21. Zaslavsky G M *Stokhastichnost' Dinamicheskikh Sistem* (Stochasticity of Dynamical Systems) (Moscow: Nauka, 1984)
22. Gutzwiller M C *Chaos in Classical and Quantum Mechanics* (New York: Springer-Verlag, 1990)
23. Reichl L E *The Transition to Chaos: Conservative Classical Systems and Quantum Manifestations* (New York: Springer-Verlag, 1992) [Translated into Russian (Moscow–Izhevsk: RKhD, 2008)]
24. Koshel K V, Prants S V *Usp. Fiz. Nauk* **176** 1177 (2006) [*Phys. Usp.* **49** 1151 (2006)]
25. Koshel' K V, Prants S V *Khaoticheskaya Advektsiya v Okeane* (Chaotic Advection in the Ocean) (Moscow–Izhevsk: RKhD, Inst. Komp'yut. Issled., 2008)
26. Zaslavsky G M, Sagdeev R Z *Vvedenie v Nelineinuyu Fiziku. Ot Mayatnika do Turbulentnosti i Khaosa* (Moscow: Nauka, 1988); *Nonlinear Physics: from the Pendulum to Turbulence and Chaos* (Chur: Harwood Acad. Publ., 1988)
27. Lichtenberg A J, Lieberman M A *Regular and Stochastic Motion* (New York: Springer-Verlag, 1983) [Translated into Russian (Moscow: Mir, 1984)]
28. Brown M G, Viechnicki J *J. Acoust. Soc. Am.* **104** 2090 (1998)
29. Brown M G et al. *J. Acoust. Soc. Am.* **113** 2533 (2003)
30. Smirnov I P, Virovlyansky A L, Zaslavsky G M *Phys. Rev. E* **64** 036221 (2001)
31. Makarov D V, Uleysky M Yu, Prants S V *Chaos* **14** 79 (2004)
32. Smirnov I P, Virovlyansky A L, Zaslavsky G M *J. Acoust. Soc. Am.* **117** 1595 (2005)
33. Flatté S M (Ed.) *Sound Transmission Through a Fluctuating Ocean* (Cambridge: Cambridge Univ. Press, 1979) [Translated into Russian (Moscow: Mir, 1982)]
34. Rytov S M, Kravtsov Yu A, Tatarskii V I *Vvedenie v Statisticheskuyu Radiofiziku* (Introduction to Statistical Radiophysics) Pt. II *Sluchainye Polya* (Random Fields) (Moscow: Nauka, 1978)
35. Virovlyansky A L, nlin/0012015
36. Virovlyansky A L *Akust. Zh.* **51** 90 (2005) [*Acoust. Phys.* **51** 71 (2005)]
37. Virovlyansky A L *Luchevaya Teoriya Dal'nego Rasprostraneniya Zvuka v Okeane* (Ray Theory of Long-Range Sound Propagation in the Ocean) (N. Novgorod: IPF RAN, 2006)
38. Leontovich M *Izv. Akad. Nauk SSSR Ser. Fiz.* **8** 16 (1944)
39. Leontovich M, Fock V *Zh. Eksp. Teor. Fiz.* **16** 557 (1946); *J. Phys. USSR* **10** 13 (1946)
40. Tappert F D *Lecture Notes Phys.* **70** 224 (1977)
41. Kravtsov Yu A, Orlov Yu I *Geometricheskaya Optika Neodnorodnykh Sred* (Geometrical Optics of Inhomogeneous Media) (Moscow: Nauka, 1980) [Translated into English (Berlin: Springer-Verlag, 1990)]
42. Landau L D, Lifshitz E M *Mekhanika* (Mechanics) (Moscow: Nauka, 1965) [Translated into English (Oxford: Pergamon Press, 1976)]
43. Makarov D, Prants S, Virovlyansky A, Zaslavsky G *Ray and Wave Chaos in Ocean Acoustics* (Singapore: World Scientific, 2010)
44. Brekhovskikh L M, Godin O A *Akustika Sloistykh Sred* (Acoustics of Layered Media) (Moscow: Nauka, 1989) [Translated into English (Berlin: Springer-Verlag, 1990, 1992)]
45. Landau L D, Lifshitz E M *Kvantovaya Mekhanika. Nerelyativistskaya Teoriya* (Quantum Mechanics. Non-Relativistic Theory) (Moscow: Nauka, 1974) [Translated into English (Oxford: Pergamon Press, 1977)]
46. Berman G P, Zaslavsky G M *Physica A* **97** 367 (1979)
47. Virovlyansky A L, Zaslavsky G M *Phys. Rev. E* **59** 1656 (1999)
48. Virovlyansky A L, Kazarova A Yu, Lyubavin L Ya *Wave Motion* **42** 317 (2005)
49. Virovlyansky A L *J. Acoust. Soc. Am.* **108** 84 (2000)
50. Colosi J A, Brown M G *J. Acoust. Soc. Am.* **103** 2232 (1998)
51. Garrett C, Munk W *Geophys. Fluid Dyn.* **3** 225 (1972)
52. Van Uffelen L J et al. *J. Acoust. Soc. Am.* **125** 3569 (2009)
53. Katsnelson B G et al. *J. Acoust. Soc. Am.* **126** EL41 (2009)
54. Badiey M et al *J. Acoust. Soc. Am.* **129** EL141 (2011)
55. Munk W, Wunsch C *Deep Sea Res. A* **26** 123 (1979)
56. Munk W, Worcester P, Wunsch C *Ocean Acoustic Tomography* (Cambridge: Cambridge Univ. Press, 1995)
57. Cornuelle B et al. *J. Phys. Oceanogr.* **15** 133 (1985)
58. Munk W, Wunsch C *Rev. Geophys. Space Phys.* **21** 777 (1983)
59. Shang E C *J. Acoust. Soc. Am.* **85** 1531 (1989)
60. Jones R M, Shang E C, Georges T M *J. Acoust. Soc. Am.* **94** 2296 (1993)
61. Udovydchenkov I A, Brown M G *J. Acoust. Soc. Am.* **123** 41 (2008)
62. Wage K E et al. *J. Acoust. Soc. Am.* **117** 1565 (2005)
63. Worcester P F et al. *J. Acoust. Soc. Am.* **105** 3185 (1999)
64. Colosi J A et al. *J. Acoust. Soc. Am.* **105** 3202 (1999)
65. Colosi J A, Tappert F, Dzieciuch M *J. Acoust. Soc. Am.* **110** 163 (2001)
66. Worcester P F et al. *J. Acoust. Soc. Am.* **95** 3118 (1994)
67. Colosi J A, Flatté S M, Bracher C *J. Acoust. Soc. Am.* **96** 452 (1994)
68. Akulichev V A et al. *Dokl. Ross. Akad. Nauk* **417** 693 (2007) [*Dokl. Earth Sci.* **417** 1432 (2007)]
69. Bezotvetnykh V V et al. *Akust. Zh.* **55** 374 (2009) [*Acoust. Phys.* **55** 376 (2009)]
70. Spindel R C et al. *IEEE J. Ocean. Eng.* **28** 297 (2003)
71. Baggeroer A B et al. (ATOC Consortium) *Science* **281** 1327 (1998)
72. Chirikov B V *Phys. Rep.* **52** 263 (1979)
73. Beron-Vera F J, Brown M G *J. Acoust. Soc. Am.* **114** 123 (2003)
74. Beron-Vera F J, Brown M G *J. Acoust. Soc. Am.* **115** 1068 (2004)
75. Morozov A D *Rezonansy, Tsikly i Khaos v Kvazikonservativnykh Sistemakh* (Resonances, Cycles and Chaos in Quasiconservative Systems) (Izhevsk: RKhD, 2005)
76. Budyansky M V, Uleysky M Yu, Prants S V *Phys. Rev. E* **79** 056215 (2009)
77. Uleysky M Yu, Budyansky M V, Prants S V *Phys. Rev. E* **81** 017202 (2010)
78. Uleysky M Yu, Budyansky M V, Prants S V *Zh. Eksp. Teor. Fiz.* **138** 1175 (2010) [*JETP* **111** 1039 (2010)]
79. Rypina I I et al. *Phys. Rev. Lett.* **98** 104102 (2007)
80. Brekhovskikh L M et al. *Akust. Zh.* **36** 824 (1990) [*Sov. Phys. Acoust.* **36** 461 (1990)]
81. Goncharov V V, Kurtepov V M *Akust. Zh.* **40** 773 (1994) [*Acoust. Phys.* **40** 685 (1994)]
82. Smirnov I P, Caruthers J V, Khil'ko A I *Izv. Vyssh. Uchebn. Zaved. Radiofiz.* **42** 982 (1999) [*Radiophys. Quantum Electron.* **42** 864 (1999)]
83. Petukhov Yu V *Acoust. Phys.* **55** 785 (2009)
84. Kudo K, Monteiro T S *Phys. Rev. E* **77** 055203(R) (2008)
85. Chuprov S D, in *Akustika Okeana. Sovremennoe Sostoyanie* (Ocean Acoustics. Current State) (Exec. Eds L M Brekhovskikh, I B Andreeva) (Moscow: Nauka, 1982) p. 71
86. Grachev G A *Akust. Zh.* **39** 67 (1993) [*Acoust. Phys.* **39** 33 (1993)]
87. Brown M G et al. *J. Acoust. Soc. Am.* **117** 1607 (2005)

88. Stöckmann H-J *Quantum Chaos*: *An Introduction* (Cambridge: Cambridge Univ. Press, 2000) [Translated into Russian (Moscow: Fizmatlit, 2004)]
89. Smirnov I P et al. *Phys. Rev. E* **72** 026206 (2005)
90. Berman G P, Kolovskii A R *Usp. Fiz. Nauk* **162** (4) 95 (1992) [*Phys. Usp.* **35** 303 (1992)]
91. Tatarskii V I *Usp. Fiz. Nauk* **139** 587 (1983) [*Sov. Phys. Usp.* **26** 311 (1983)]
92. Virovlyansky A L, Zaslavsky G M *Chaos* **15** 023301 (2005)
93. Bäcker A, Ketzmerick R, Monastra A G *Phys. Rev. Lett.* **94** 054102 (2005)
94. Heller E J *Phys. Rev. Lett.* **53** 1515 (1984)
95. Itin A P, Neishtadt A I, Vasiliev A A *Physica D* **141** 281 (2000)
96. Neishtadt A I *Tr. Steklov Mat. Inst.* **250** 198 (2005) [*Proc. Steklov Inst. Math.* **250** 183 (2005)]
97. Neishtadt A, Vasiliev A *Nonlinearity* **18** 1393 (2005)
98. Vainchtein D L, Neishtadt A I, Mezic I *Chaos* **16** 043123(2006)
99. Leoncini X, Neishtadt A, Vasiliev A *Phys. Rev. E* **79** 026213 (2009)
100. Bogoliubov N N, Mitropolsky Y A *Asimptoticheskie Metody v Teorii Nelineinykh Kolebanii* (Asymptotic Methods in the Theory of Non-Linear Oscillations) (Moscow: Fizmatlit, 1958) [Translated into English (Delhi: Hindustan Publ. Corp., 1961)]
101. Makarov D V, Uleysky M Yu *Commun. Nonlin. Sci. Numer. Simul.* **13** 400 (2008)
102. Makarov D V, Uleyskiy M Yu *Akust. Zh.* **53** 565 (2007) [*Acoust. Phys.* **53** 495 (2007)]
103. Makarov D V, Kon'kov L E, Uleysky M Yu *Akust. Zh.* **54** 439 (2008) [*Acoust. Phys.* **54** 382 (2008)]
104. Neishtadt A, Vasiliev A *Chaos* **17** 043104 (2007)
105. Makarov D V, Sosedko E V, Uleysky M Yu *Eur. Phys. J. B* **73** 571 (2010)
106. Uleysky M Yu, Budyansky M V, Prants S V *J. Phys. A Math. Theor.* **41** 215102 (2008)
107. Grigorieva N S, Fridman G M, Palmer D R *J. Comput. Acoust.* **12** 355 (2004)
108. Hegewisch K C, Cerruti N R, Tomsovic S *J. Acoust. Soc. Am.* **117** 1582 (2005)
109. Kon'kov L E et al. *Phys. Rev. E* **76** 056212 (2007)
110. Leboeuf P, Voros A *J. Phys. A Math. Gen.* **23** 1765 (1990)
111. Makarov D V, Kon'kov L E *Nelineinaya Dinamika* **3** 157 (2007)
112. Makarov D V, Kon'kov L E, Uleysky M Yu *Zh. Sib. Fed. Univ. Ser. Mat. Fiz.* **3** 336 (2010)
113. Keating J P, Prado S D *Proc. R. Soc. Lond. A* **457** 1855 (2001)
114. Kulkarny V A, White B S *Phys. Fluids* **25** 1770 (1982)
115. Klyatskin V I, Gurarie D *Usp. Fiz. Nauk* **169** 171 (1999) [*Phys. Usp.* **42** 165 (1999)]
116. Froyland G et al. *Phys. Rev. Lett.* **98** 224503 (2007)
117. Bódai T, Fenwick A J, Wiercigroch M *J. Sound Vibr.* **324** 850 (2009)
118. Makarov D, Uleysky M *J. Phys. A Math. Gen.* **39** 489 (2006)
119. Makarov D V et al. *Phys. Rev. E* **73** 066210 (2006)
120. Gan C, Wang Q, Perc M *J. Phys. A Math. Theor.* **43** 125102 (2010)
121. Kolovsky A R *Phys. Rev. E* **56** 2261 (1997)
122. Zaslavskii G M *Usp. Fiz. Nauk* **129** 211 (1979) [*Sov. Phys. Usp.* **22** 788 (1979)]
123. Berry M V, Robnik M *J. Phys. A Math. Gen.* **17** 2413 (1984)
124. Izrailev F M *Phys. Rep.* **196** 299 (1990)
125. Brody T A *Lett. Nuovo Cimento* **7** 482 (1973)
126. Berry M V, Keating J P, Prado S D *J. Phys. A Math. Gen.* **31** L245 (1998)
127. Berry M V, Keating J P, Schomerus H *Proc. R. Soc. Lond. A* **456** 1659 (2000)
128. Virovlyanskii A L, Zaslavskii G M *Akust. Zh.* **53** 329 (2007) [*Acoust. Phys.* **53** 282 (2007)]
129. Virovlyansky A L, Kazarova A Yu, Lyubavin L Ya *J. Acoust. Soc. Am.* **121** 2542 (2007)
130. Virovlyansky A L, Kazarova A Yu, Lyubavin L Ya *J. Acoust. Soc. Am.* **125** 1362 (2009)
131. Colosi J A, Flatté S M *J. Acoust. Soc. Am.* **100** 3607 (1996)
132. Virovlyansky A L *Izv. Vyssh. Uchebn. Zaved. Radiofiz.* **46** 555 (2003) [*Radiophys. Quantum Electron.* **46** 502 (2005)]
133. Tikhonov V I, Mironov M A *Markovskie Protsessy* (Markov Processes) (Moscow: Sovetskoe Radio, 1977)
134. Gardiner C W *Handbook of Stochastic Methods for Physics, Chemistry, and the Natural Sciences* (Berlin: Springer-Verlag, 1985) [Translated into Russian (Moscow: Mir, 1986)]
135. Rypina I I, Brown M G *J. Acoust. Soc. Am.* **122** 1440 (2007)
136. Vadov R A *Akust. Zh.* **52** 448 (2006) [*Acoust. Phys.* **52** 377 (2006)]
137. Dushaw B D *IEEE J. Ocean. Eng.* **24** 215 (1999)
138. Spiesberger J L, Metzger K *J. Geophys. Res.* **96** (C3) 4869 (1991)
139. Virovlyansky A L *J. Acoust. Soc. Am.* **113** 2523 (2003)
140. Virovlyansky A L *Akust. Zh.* **51** 330 (2005) [*Acoust. Phys.* **51** 271 (2005)]
141. Virovlyansky A L, Zaslavsky G M *Chaos* **10** 211 (2000)
142. Morozov A K, Colosi J A *Akust. Zh.* **51** 386 (2005) [*Acoust. Phys.* **53** 335 (2007)]